nature reviews materials

https://doi.org/10.1038/s41578-024-00729-3

Review article

Check for updates

Decoding tissue biomechanics using conformable electronic devices

Hyeokjun Yoon[1,3], Jin-Hoon Kim[1,3], David Sadat[1], Arjun Barrett[1], Seung Hwan Ko[2] & Canan Dagdeviren[1]

Abstract

Understanding the human body's tissue biomechanics — the physical deformation and variations in intrinsic mechanical properties — has considerable potential in health monitoring, disease diagnosis and bioengineering. However, current tools for decoding tissue biomechanics rely on rigid and bulky devices that are not compatible with biological tissues. Such a discrepancy results in inaccurate measurement and even pain and discomfort for the subjects undergoing the measurement. To overcome the limitations of current tools, conformable electronic devices have been developed for monitoring internal and external tissue biomechanics. Moreover, by adopting advanced machine-learning approaches, more insights can be gained from the collected data. In this Review, we provide a comprehensive overview of conformable electronic devices for tissue biomechanics decoding. We discuss basic principles for external and internal tissue decoding, focusing on electromechanical transduction for external tissue decoding and on ultrasonography for internal tissue decoding. Then, we highlight various data analysis methods, including machine-learning algorithms. Finally, we outline challenges and future directions.

Sections

[1]Media Lab, Massachusetts Institute of Technology, Cambridge, MA, USA. [2]Applied Nano and Thermal Science Lab, Department of Mechanical Engineering, Seoul National University, Seoul, Republic of Korea. [3]These authors contributed equally: Hyeokjun Yoon, Jin-Hoon Kim. e-mail: canand@media.mit.edu

Introduction

Tissue biomechanics refers to the mechanical dynamics of the human body and to the spatiotemporal variability of the intrinsic mechanical properties of biological tissues[1]. Such tissue biomechanics reflects the biological status of the human body, including body motion, cardiorespiratory function, disease progression, verbal activities, rehabilitation and internal organs dynamics (Box 1). Hence, decoding the tissue biomechanics of the human body has considerable potential in various biomedical applications including regular health monitoring[2,3], disease diagnosis[4–6], rehabilitation[7,8], robotics[9,10], augmented reality (AR), virtual reality (VR)[11] and wearable point-of-care therapy[12].

However, the decoding of tissue biomechanics faces several fundamental challenges related to long-term usage, signal accuracy, comfortability and safety, owing to the inherent mechanical mismatch between the current measurement tools and biological tissues (Box 2). Conventional devices for tissue biomechanics decoding are usually rigid, bulky, expensive, unamenable and require mechanical pressure to maintain contact, which can cause pain and distort measurements[13]. Some of the conventional tools used for decoding internal tissue biomechanics, such as computed tomography and mammography, also involve radiation exposure, which is potentially harmful for regular medical usage (Table 1). Moreover, as these tools are expensive and not portable, individuals are required to visit medical institutes in-person, which limit frequent monitoring, especially in developing countries and rural areas[14].

In this regard, soft miniaturized devices with wearable form factors have gained considerable interest for the decoding of external and/or internal tissue biomechanics in real-time in a portable, convenient and non-invasive manner[15] (Table 1). To accurately monitor tissue biomechanics without the need for excessive mechanical pressure or support from professionals, maintaining good conformable contact with the tissue is extremely critical (Box 2). With advances in materials, device design and analysis techniques, wearable electronic devices can maintain good conformability and have been used in several successful demonstrations (Table 1). The current state-of-the-art devices now show comparable performance with conventional rigid, bulky and expensive devices[6,16].

Advanced machine-learning algorithms can also be leveraged to gain deeper insights from the collected data[17,18]. Such analysis techniques have been used to accurately reflect biomechanical information, with applications in motion classification, vocal-less communication, health monitoring and disease diagnosis.

In this Review, we discuss the basic principles and current progress of conformable wearable devices for decoding external and internal tissue biomechanics. We divide the discussion into two areas: outside and inside the body, based on the decoding target. We elaborate on various fundamental sensing mechanisms, materials and structure design for realizing highly functional conformable devices, focusing on electromechanical transduction mechanisms for external tissue decoding and on ultrasonography for internal tissue decoding. In addition, we present cutting-edge data analysis strategies including machine-learning-based approaches and sensor fusion methods. As examples, we investigate state-of-the-art biomedical applications. Finally, we suggest current challenges and future perspectives towards the development of fully portable and practical wearable devices for tissue biomechanics decoding.

Decoding external tissue biomechanics

The main targets for external tissue biomechanics decoding are the skin, which mainly reflects the dynamics of the joints and muscles, and the mechanical vibrations (for example vocal, cardiovascular or respiratory) of the human body. Effectively decoding external tissue biomechanics requires innovative materials and device designs to obtain high sensitivity, a wide operational range and good reliability[19,20].

Principles of external tissue biomechanics decoding

The main strategy for decoding external tissue biomechanics is direct electromechanical transducing, that is, the conversion of mechanical deformation into electrical signals (Fig. 1). When biological tissues are subjected to external mechanical deformation, conformably attached sensors can accurately detect such deformations by converting them into electrical signals (changes in voltage, current or resistance)[21]. Other external biomechanics sensing methods, such as optical (through the monitoring of light intensity or resonance frequency changes upon deformation) and inertial measurement units (through the monitoring of acceleration and changes in orientation of the tissue upon deformation), have been demonstrated and are detailed in Supplementary Note 1.

Piezoresistivity. Piezoresistivity denotes electrical resistance changes upon mechanical deformation or stress. This effect comes from various fundamental mechanisms including modification of the band gap, changes in geometry and modifications of the conduction path[22,23] (Fig. 1).

In semiconducting materials such as Si and Ge, the band gap can be modified by external strain owing to conduction band splitting, which can enhance the carrier mobility[24]. An example device exploiting piezoresistivity by band gap modification is the microfabricated ultrathin Si nanomesh, which has been adopted as a conformable strain gauge to monitor small strains[25]. Although inorganic semiconducting material-based strain sensors have high sensitivity, intrinsic brittleness of inorganic materials limits their application to the measurement of small strains, whereas conformable devices typically operate under high strains (>30%). To overcome the intrinsic brittleness of inorganic semiconducting materials, various other piezoresistive mechanisms and structure modifications have been considered.

When thin metal films are stretched beyond their failure strain, microcracks start to form, which results in piezoresistivity[26]. These microcracks are closed and a portion of the conduction path is restored when the applied strain is released (Fig. 1a). Such reversible disconnection and connection of microcracks upon mechanical deformation can be used to decode external tissue biomechanics.

Various multidimensional nanomaterials including nanoparticles, nanowires, nanotubes and nanosheets have also been utilized as building blocks for flexible, stretchable and transparent electrodes[27–29]. Because the physical contact between each nanomaterial is maintained by very weak van der Waals interactions, the electrical conduction path formed by networks of nanomaterials can easily be affected by external mechanical deformation (Fig. 1b). In that case, the electrical conduction relies on tunnelling, which is highly dependent on the distance between nanomaterials[30]:

$$R_{\text{tunnel}} = \frac{h^2 d}{Ae^2\sqrt{2m\lambda}} \exp\left(\frac{4\pi d}{h}\sqrt{2m\lambda}\right) \quad (1)$$

in which e is a quantum of electricity, m the electron mass, h Planck's constant, d the distance between nanomaterials, λ the energy barrier height of the dielectric medium through which the electrons should tunnel and A the cross-sectional area of the tunnel[30].

Box 1 | Decoding tissue biomechanics

Representative targets of biomechanics studies comprise strain, pressure, modulus and motion (dynamics)[1], which can reflect the physiological state and functionality of soft tissues. Such information is invaluable for various biomedical applications including health monitoring, medical diagnosis and treatment. The target tissues for biomechanics decoding can be divided into external envelope (skin) and internal organs[5] (see the figure).

Here, we define external tissue biomechanics as the mechanics decoded from the skin. Because skin deforms with various body motions, accompanying a wide range of strain, skin biomechanics is effective for the motion detection of various body parts. Additionally, because the skin deforms during speech, it can be used for speech recognition and vocal-less communication by decoding pressure from high frequency vibration. Furthermore, the modulus of the skin can aid in diagnosing and monitoring skin diseases. Finally, by evaluating the strain or pressure of the skin over blood vessels, blood pulses can be decoded through the deformation of the skin.

Internal tissue biomechanics comprises the biomechanics of inner organs and muscles. Organ dynamics, which generally denotes organ movement or volume change, is directly related to the functionalities of the organs including the heart, bladder, lung, diaphragm, muscle and blood vessels. Moreover, organ characteristics also reflect the health status of the tissues. Diseases from various organs including the liver, lung and pancreas can be detected through the assessment of their elastic modulus. Furthermore, tissue anomaly can be detected as anomalies including lesion and tumour have distinguishable modulus. Finally, beyond simple body vital sign measurements, the decoding of spatial or volumetric blood flow configuration is also possible.

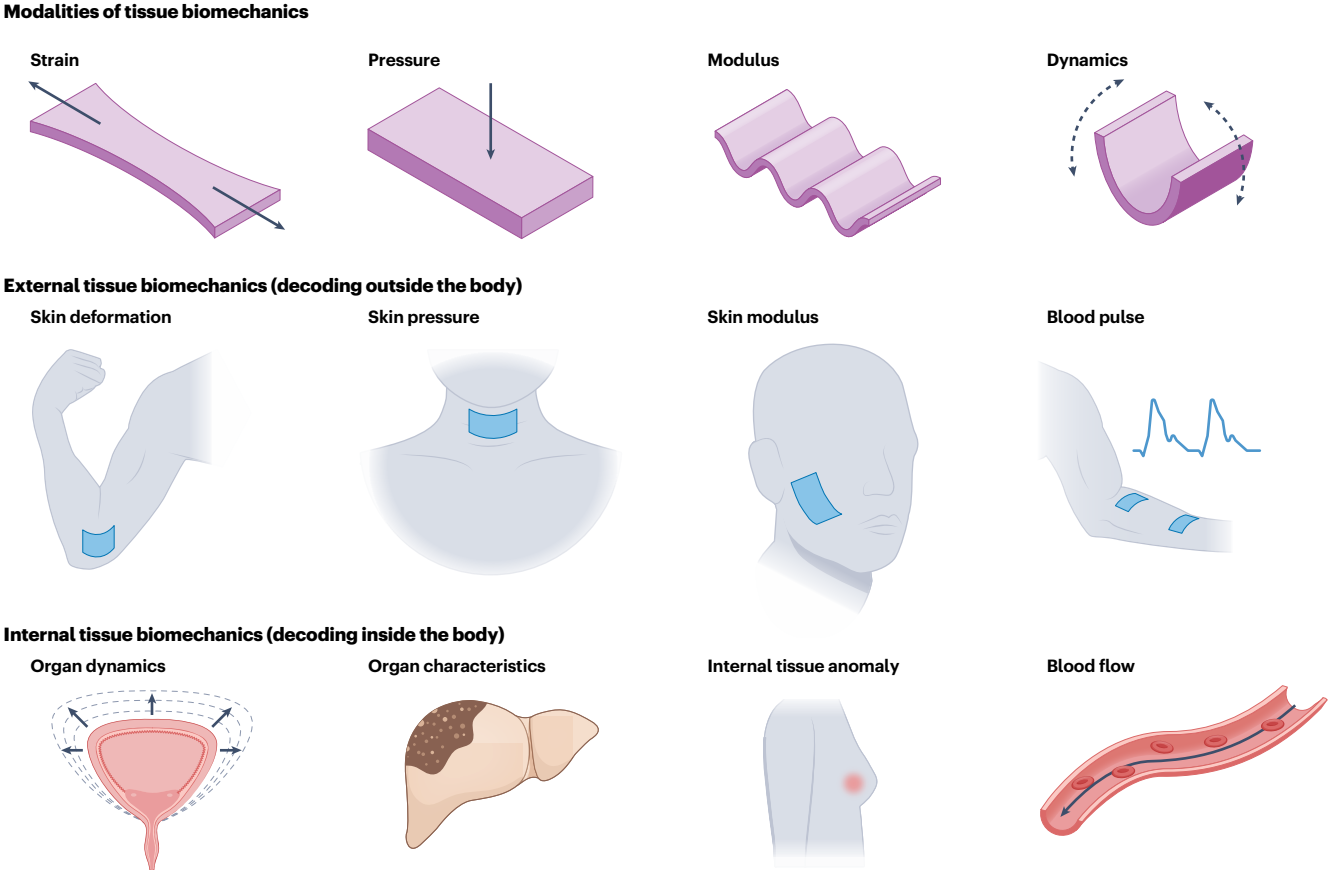

Piezocapacitivity and iontronics. Another approach to decode external tissue biomechanics is based on capacitance measurements. When a capacitor — composed of a dielectric layer sandwiched between two conductive plates (Fig. 1c) — is pressed or stretched, its capacitance changes owing to geometrical changes (contact area and thickness of the dielectric layer), leading to the piezocapacitive effect[7,31]:

$$C = \varepsilon_r \varepsilon_0 \frac{A}{d} \quad (2)$$

in which ε_r and ε_0 are the permittivities of the dielectric layer and of free space, respectively, A is the area of one of the plates and d is the distance between the two plates. Capacitance measurements are resilient to

mechanical deformations and are independent of temperature and humidity[18]. However, the sensitivity of piezocapacitive devices is generally lower than that of piezoresistive devices as it only depends on geometrical changes in the capacitor structure[32], whereas in piezoresistive devices other mechanisms including percolation network changes are also affected by the mechanical deformation[33].

To cope with the limitations of piezocapacitive devices, iontronic devices have been proposed. In iontronic devices, mobile ions are present in the dielectric layer (Fig. 1d). The major difference between piezocapacitive and iontronic sensors is that the mobile ions form an additional electric double layer at the interface between the electrodes and the ionic medium, which increases the capacitance of the device. Such electric double layers have ultrahigh unit area capacitance of the order of several microfarads per square centimetre, around three to four orders of magnitude higher than traditional parallel plate capacitors[34] (Fig. 1c). Such high capacitance

Box 2 | Conformable decoding

To obtain accurate information through conformable devices with minimum noise, motion artefacts and delamination, maintaining good conformable contact is extremely important[269–271]. Conformability in wearable electronics refers to maintaining seamless contact with biological tissues without delaminating during dynamic motion. Conventional materials used to fabricate electronic devices have a Young's modulus several orders of magnitude higher than biological tissues (see the figure, panel **a**). Even polymers used for substrates (polyimide (PI), SU-8 and polydimethylsiloxane (PDMS)) have a higher Young's modulus than most biological tissues. To increase conformability, two main strategies have been developed. The first approach is developing devices with soft materials including hydrogels and conjugated polymers. Another approach is structurally modifying devices made with conventional materials. The conformability of devices not only depends on the Young's modulus but also on the bending stiffness of the structure, which is proportional to the Young's modulus and to the cube of the thickness of the structure[272,273]. Hence, if the total structure is thinner than a certain threshold thickness, the device can maintain conformal contact with soft biological tissues (see the figure, panel **b**). In this Review, we mainly focus on the second approach. Good adhesion with biological tissues is also an important factor to maintain conformability. Although devices with a thin geometry can maintain conformable contact with biological tissues through van der Waals interactions, stronger adhesion mechanisms are required for accurate positioning and long-term monitoring without delamination (see the figure, panel **c**).

PEDOT:PSS, poly(3,4-ethylenedioxythiophene)-poly(styrenesulfonate); PVDF, polyvinylidene fluoride; PZT, lead–zirconate–titanate. Information contained in panel **a** is from refs. 230,274–281. Panel **b** reprinted with permission from ref. 282, Wiley.

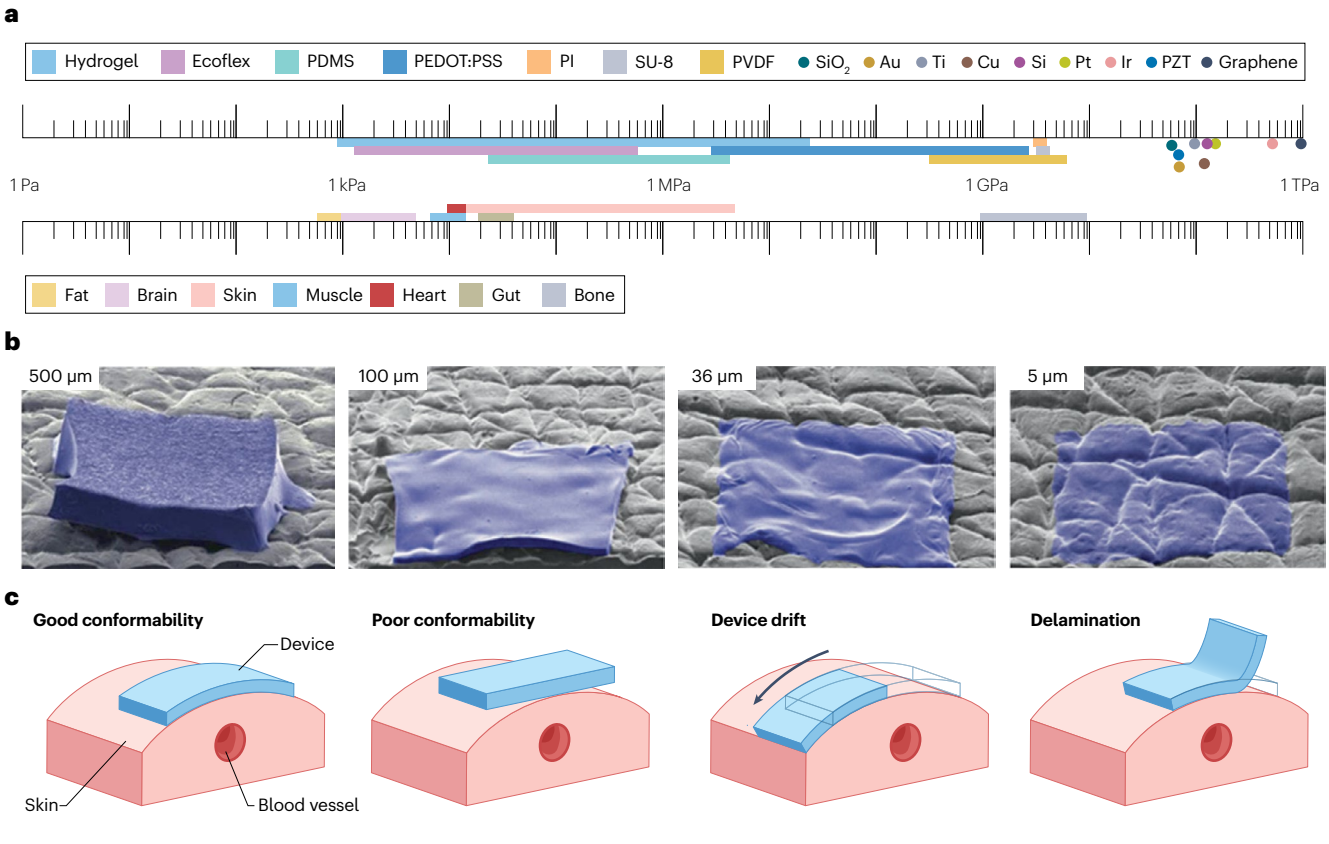

Table 1 | Decoding targets and comparison of corresponding conventional tools and conformable devices

Decoding target	Categories	Conventional tools	Limitations	Mechanisms of conformable devices	Characteristics of conformable devices
Body motion	External tissue decoding	Motion capture cameras IMU, accelerometer and gyroscope	Expansive, bulky and limited dimensionality (cameras) Low accuracy due to drift and frequent calibration required (IMU)[244]	Combination of multiple sensing mechanisms (nanomaterial percolation network and microcrack propagation) Optical fibre	High deformation range: bending angle of 140° for knee joints[245] and 90° for finger joints[246] System can be miniaturized and device conformability
	Internal tissue decoding	EMG	Modification of the signal after muscle fatigue (EMG)[247] Needle-type invasive electrodes required (EMG)	Ultrasound imaging with A and B mode	Frequency of ultrasound waves: ~6.5 MHz (ref. 186) Depth of penetration: ~50 mm (ref. 186)
Cardiovascular activity	External	Cuff	Bulky and uncomfortable, improper for continuous monitoring (cuff)[215]	Pressure sensing with piezoelectric, triboelectric and capacitive mechanisms	High sensitivity: over 500 Pa^{-1} (ref. 248)
	Internal	Ultrasound imaging machine PPG ECG	Large and bulky (ultrasound imaging machine)[6] Professional operator needed (ultrasound imaging machine)[6] Sensitive to skin colours, contact pressure and motion artefacts (PPG)[249] Large motion artefact and accurate positioning of electrodes required (ECG)	Ultrasound imaging with A, B, M and Doppler mode Photoacoustic imaging Electromagnetic sensing mechanism	Frequency: ~2 MHz (ref. 122) Depth: ~15 cm (ref. 122); frequency: ~2.5 MHz (ref. 250) Depth: <30 mm (ref. 250) Implantable sensing devices needed in some cases[251]
Speech recognition	External	Microphone	Limited in noisy environments[177]	Pressure sensing with piezoelectric and piezoresistive mechanism	Wide range of operational frequencies: response time less than 10 ms for facile motion detection[90] and more than 1 kHz for vocal cord vibration monitoring[177,217,218]
Skin modulus	External	In situ indentation, tensile, suction and torsion tests	Large and bulky[5] Not suitable for continuous monitoring	Lateral acoustic wave propagation and reception Electromagnetic sensing mechanism	Uses actuator–sensor pairs[5] Magnet-induced vibration and strain gauge sensing[4]
	Internal	MRE[179]	Large and bulky[179]	Ultrasound imaging with B and transmission mode	Frequency: ~3 MHz (ref. 179) Depth: ~40 mm (ref. 179)
Organ movement	Internal	Ultrasound imaging machine Implantable devices	Large and bulky (ultrasound imaging machine) Professional operator needed (ultrasound imaging machine) Operation needed to implant devices (implantables)	Ultrasound imaging with A, B, M and Doppler mode Mechano-acoustic sensing mechanism	Frequency: ~3 MHz (ref. 118) Depth: 2–12 mm (ref. 118) Can be used for signals from different organs including the heart, lungs and the intestine with signal decomposition
Organ characteristics	Internal	Ultrasound imaging machine MRI CT	Large and bulky (all) Professional operator needed (all) Radiation from the machine (CT)	Ultrasound imaging with A, B, M and Doppler mode	Frequency: ~7.5 MHz (ref. 219) Depth: 40–60 mm (ref. 219)
Organ volume	Internal	Ultrasound imaging machine MRI CT	Large and bulky (all) Professional operator needed (all) Radiation from the machine (CT)	Ultrasound imaging with B mode	Frequency: ~3.5 MHz (ref. 106) Depth: ~15 cm (ref. 106)
Muscle activity	Internal	EMG MRE[179]	Modification of the signal after muscle fatigue (EMG) Large and bulky (MRE)	Ultrasound imaging with A, B, M and Doppler mode	Frequency: ~3 MHz (ref. 179) Depth: ~40 mm (ref. 179)
Tissue anomaly	Internal	Palpation Mammography MRI CT Ultrasound imaging machine	Inaccuracy (palpation) Large and bulky (mammography, MRI, CT, ultrasound imaging machine) Radiation from the machine (mammography, CT) Professional operator needed (all)	Ultrasound imaging with B mode	Frequency: ~7 MHz (ref. 6) Depth: ~80 mm (ref. 6)

A mode, amplitude mode; B mode, brightness mode; CT, computed tomography; ECG, electrocardiography; EMG, electromyography; IMU, inertial measurement unit; M mode, motion mode; MRE, magnetic resonance elastography; MRI, magnetic resonance imaging; PPG, photoplethysmography.

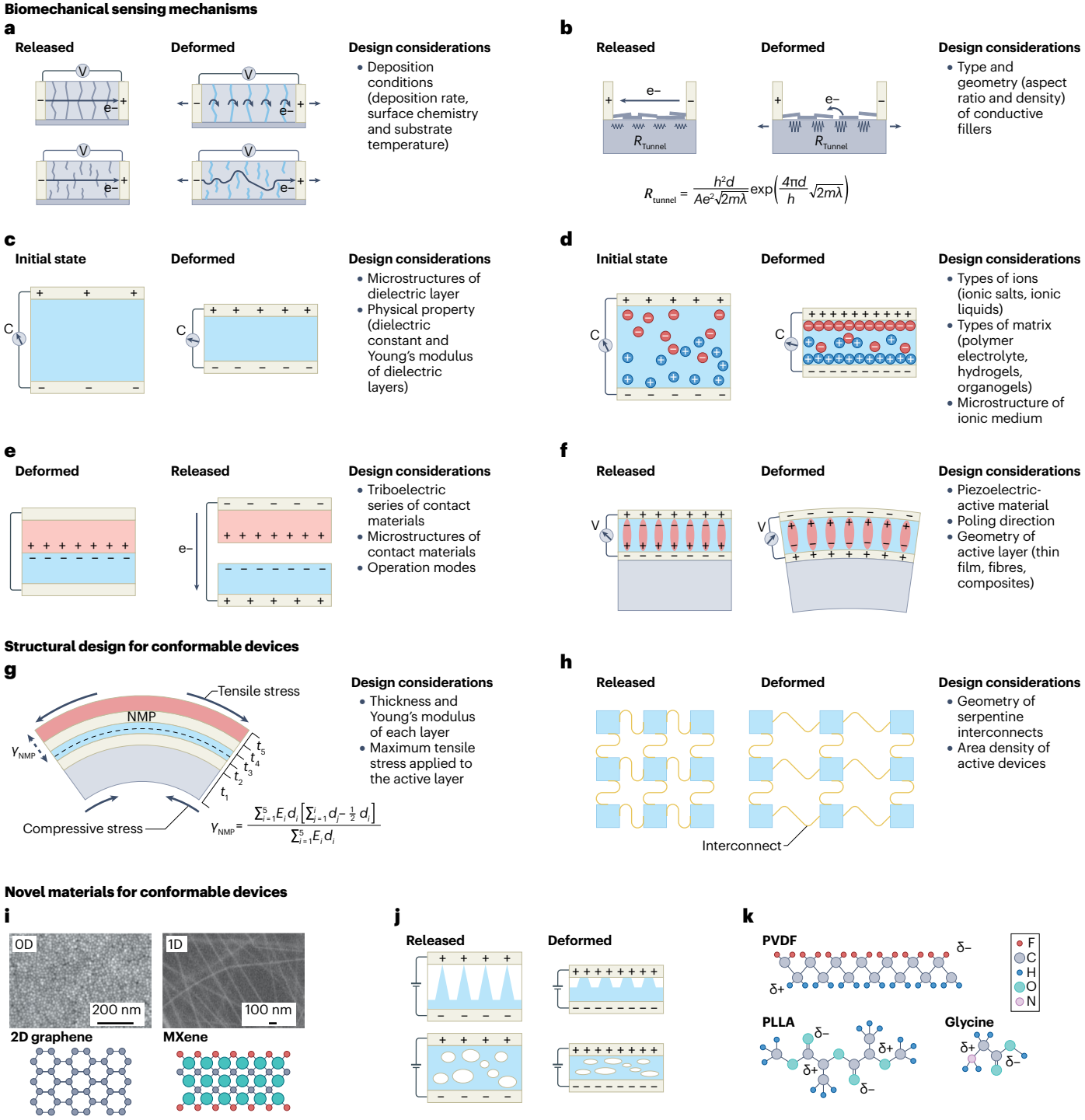

can provide ultrahigh sensitivity and resolution for a wide range of pressures[35].

Triboelectricity. The triboelectric effect has become one of the most important mechanisms for power generation and sensing in wearable devices[36,37]. When two different materials are put in contact, charge transfer occurs at the interface[38] (Fig. 1e). Electron transfer at the interface is mainly caused by the work function difference between the materials[38], in which electrons move from materials with higher work functions to materials with lower work function[39]. Mobile ions can also move across the interface. Adsorbed water molecules on the surface contribute to ion transfer by spontaneously forming H^+ and OH^- ions[38]. Material transfer can also occur during electrification, which contributes to charge transfer reactions in triboelectric devices[38,40]. When two contacted materials are separated or sheared against each other, an electrical field is generated by the separation of charges. By utilizing

Fig. 1 | Mechanisms of external tissue biomechanics decoding. a, Mechanism (left) and design considerations (right) for conformable devices using microcrack engineering. When large channel cracks are formed during mechanical deformation, the electrical resistivity increases substantially even at low strain (<10%) owing to disrupted conduction channels. Although when small microcracks are formed, electrical conduction path can be maintained, resulting in minimal increase in electrical resistance. **b**, Mechanism (left) and design considerations (right) for conformable devices using multidimensional nanomaterials. The piezoresistive sensing mechanism is illustrated for 1D nanowire-based devices. Changes in the tunnelling distance between nanomaterials induce a change in the electrical resistance of the device, as shown in the equation. **c**, Mechanism (left) and design considerations (right) for piezocapacitive devices. The deformation of the dielectric layer induces a capacitance change. **d**, Mechanism (left) and design considerations (right) for iontronic devices. The formation of an electrical double layer at the ionic medium–electrode interface can substantially increase the capacitance of the device. **e**, Mechanism (left) and design considerations (right) for triboelectric devices. The charge transfer between two different materials during contact induces an electric field across two electrodes, which results in voltage difference or electrical current between the electrodes. **f**, Mechanism (left) and design considerations (right) for piezoelectric devices. Mechanical deformations such as bending and pressing induce lattice distortion to the piezoelectric materials, which result in the formation of an electrical field between the two electrodes sandwiching the piezoelectric thin film. **g**, Mechanism (left) and design considerations (right) of the neutral mechanical plane (NMP) design in multilayered thin films. The NMP in a multilayered system is determined by the Young's modulus and the thickness of the components. **h**, Mechanism (left) and design considerations (right) of the serpentine interconnect method. Mechanical strain applied to the devices is mainly induced to the serpentine interconnects, hence minimizing the stress induced to the active device components. **i**, Various types of multidimensional nanomaterials for conformable electronics. Scanning electron microscopy image of (top right) 0D nanoparticles and (top left) 1D nanowires (top right) deposited on the substrate. Schematic illustration of 2D materials (bottom). **j**, Various microstructured layers for enhancing sensing performance. Schematic illustration of micropyramidal (top) and porous (bottom) dielectric layers under mechanical deformation. Such microstructured dielectric layers are widely used to increase the sensitivity of multiple sensing mechanisms including piezocapacitivity, iontronic sensing and triboelectricity. **k**, Examples of organic piezoelectric materials. Schematic illustration of organic piezoelectric materials. Functional groups with high polarity contribute to the piezoelectric performance of organic materials. PLLA, poly(L-lactic acid); PVDF, polyvinylidene fluoride. For definitions of other variables, see the main text. Panel **i** (left) reprinted from ref. 57, CC BY 4.0. Panel **i** (right) reprinted with permission from ref. 230, American Chemical Society.

diverse device design strategies, the triboelectric mechanism can be utilized to measure tissue biomechanics[41,42].

Piezoelectricity. Another major sensing mechanism for tissue biomechanics decoding is piezoelectricity, which harnesses the charge accumulation exhibited by certain types of materials upon mechanical deformation or stress[43,44]. Piezoelectric materials usually have an asymmetric unit cell, polar axis and no inversion symmetry in their crystal structure, which makes the charge neutralization of the system easily disturbed[45]. Hence, when piezoelectric materials are mechanically deformed, a large amount of charge can be generated owing to polarization, which is called a direct piezoelectric effect (Fig. 1f). Conformable devices based on piezoelectric materials also have a capacitor-type structure (Fig. 1f). When the mechanical deformation is applied to piezoelectric devices, an electric field is generated. A detailed theoretical discussion for the output voltage under mechanical deformation is discussed in Supplementary Note 2. Conversely, when an electric field is applied to the piezoelectric material, a mechanical deformation can be induced, which is called a converse piezoelectric effect. Both mechanisms can be efficiently utilized in conformable devices.

Materials, structures and design criteria for external tissue biomechanics decoding

Various mechanisms have been developed to decode external tissue biomechanics using conformable devices. A key challenge in this area involves selecting suitable materials and designing device structures that enable accurate and efficient biomechanical decoding. These considerations are critical to the performance and reliability of conformable devices in practical applications.

Piezoresistive devices. The most fundamental mechanism of piezoresistivity is electronic band structure tuning owing to mechanical deformation. Although semiconducting materials such as Si have good piezoresistive properties, their intrinsic brittleness limits their effectiveness when applied to conformable devices. Hence, various strategies have been developed to enable conformable contact between semiconducting inorganic materials and biological tissues[46]. The first approach is to use ultrathin (<100 nm) semiconducting films with thin substrates (<10 μm). The deformation and stress distribution of 'plates' under external forces or bending moments can be calculated using the plate bending theory. According to this theory, the stress applied to thin films is proportional to the total thickness of the device and bending radius[47]. For instance, if the total thickness of the Si is less than 10 μm, the tensile strain applied to the Si is around 0.7% under a bending radius of 1 mm, which is lower than the failure strain of Si (about 1%)[48], which indicates that using ultrathin film can minimize the strain applied to the inorganic semiconducting layer. To further minimize the mechanical strain applied to the specific thin film, the device structure can be engineered to place the inorganic thin film in the neutral mechanical plane (NMP) (Fig. 1g). The position of the NMP can be defined as:

$$y_{\mathrm{NMP}} = \frac{\sum_{i=1}^{n} E_i d_i \left[\sum_{j=1}^{i} d_j - \frac{d_i}{2} \right]}{\sum_{i=1}^{n} E_i d_i} \tag{3}$$

in which y_{NMP}, E_i and d_i are the position of the NMP from the top surface, Young's modulus and thickness of the ith layer, respectively[49].

Because the strategy mentioned earlier can only reduce the bending strain, another approach is required to reduce the tensile strain. For example, to reduce the applied strain during stretching, semiconducting membranes can be patterned into a smaller area and connected with serpentine interconnects called 'island–bridge' structures (Fig. 1h). By reducing the area density, the amount of strain applied to the semiconductor membrane is decreased, as most of the strain is concentrated on the serpentine interconnects.

By adopting these approaches, even brittle inorganic semiconducting materials such as Si can be conformably attached to soft biological tissues. For example, Si nanomembranes with serpentine traces placed in the NMP can be stretched up to 30% strain and show no degradation in piezoresistive property after 50,000 cycles of stretching[25]. Three-dimensional Si nanomembranes have also been

Table 2 | Comparison of different mechanisms for external biomechanics decoding

Mechanisms		Pros	Cons	Refs.
Piezoresistivity	Inorganic semiconductors	High accuracy and reliability High sensitivity at low strain range (<1% strain)	Limited to low deformation range Complicate fabrication process required	25,253
	Microcracks	Highly sensitive Simple structure and fabrication Wide working range	Difficult to control the microcrack geometry Large hysteresis External power required	254,255
	Multidimensional nanomaterials	Solution processability Wide selectivity of materials	Low repeatability Difficult to control the dimension of individual nanomaterial External power required	255,256
Piezocapacitivity		High mechanical stability Low power consumption	Limited detection range Highly vulnerable to external electromagnetic interference Crosstalk between sensing unit	256,257
Iontronicity		High sensitivity and resolution Low power consumption	Signal drifts from the viscoelastic creep of ionic gels Ionic solvent leakage and phase separation under the pressure (ionic liquid and organogels) Water evaporation (hydrogels)	34,80,258
Triboelectricity		Self-powered Wide selectivity of materials High output voltage signal	Sensitive to moisture Prone to mechanical fatigue	255,259,260
Piezoelectricity		Self-powered High sensitivity Can generate acoustic waves for various sensing mechanisms	High temperature processing required (inorganic materials) Low electromechanical conversion efficiency and acoustic pressure (organic materials) Hysteresis behaviour	256,261

investigated for decoding external soft tissues biomechanics[50]. These 3D structured devices have several advantages over conventional planar geometries including high mechanical sensitivity, insensitivity to temperature and ability to decode multiple mechanical deformations including shear stress[50]. Although such microfabricated inorganic thin film-based conformable devices have good deformability and reliable performances, this approach requires complicated fabrication processes and has a limited operational strain range (<30%)[25] (Table 2 and Supplementary Table 1).

Another strategy to design piezoresistive devices is microcrack engineering. When designing microcrack-based biomechanics sensors, the most important thing to consider is the geometry of the microcracks based on the target operational strain range[51]. If large channel cracks are formed during stretching, electrical disconnection can easily occur and electrical resistance markedly increases even when a small strain is applied (Fig. 1a). This approach is suitable for highly sensitive mechanical deformation sensing within a small operational strain range. However, if high stretchability is required, the morphology of the films can be modified to enable the propagation of a large number of small microcracks. In this scenario, the conduction paths can be maintained even under high strain (Fig. 1a). This morphology can be modified by controlling various parameters including the deposition rate, deposition temperature, substrate pretreatment and geometry[52–54] (Supplementary Note 3). Microcrack-based conformable devices are advantageous owing to their relatively simple fabrication process (vacuum deposition or solution process without photolithography) and wide operational range (Supplementary Table 1). However, owing to difficulties in controlling the microcrack geometry, achieving device-to-device uniformity is challenging (Table 2).

Nanomaterials can exhibit piezoresistive properties owing to changes in their percolation network and in the tunnelling distance between each nanomaterial. When designing nanomaterial-based piezoresistive sensors, the dimensions of the nanomaterial should be carefully selected based on target applications and corresponding deformation range. Zero-dimensional materials (Fig. 1i) are suitable for high sensitivity measurements but they have a low operational range (<10% strain) owing to their inherent low aspect ratio, which can easily lead to the disconnection of the conduction path under mechanical strain[55–58]. Owing to their high aspect ratio, 1D or 2D materials are more appropriate for measuring high deformations (Fig. 1i). One-dimensional and two-dimensional materials have several unique advantages such as a low percolation threshold, large mechanical deformability, high optical transparency, optoelectronic properties and mechanical softness[59–63]. When designing 1D and 2D nanomaterial-based biomechanics sensors, the geometry and structure of the percolation network can be optimized depending on the target deformation range and sensitivity[64], for example, by adjusting the density of the percolation network[65] or by directionally aligning the nanomaterials[66].

To achieve both high sensitivity and stretchability, multiple sensing mechanisms can be combined (Supplementary Note 4). Most widely utilized nanomaterials including Ag nanowires, Au nanoparticles, graphene and silver nanoplates can be synthesized by solution processes with a large volume[67–70] and easily processed into thin films[71,72]. However, nanomaterials have intrinsic limitations including inconsistent performance and size variability of individual nanomaterials (Table 2 and Supplementary Table 1).

Piezocapacitive and iontronic devices. Piezocapacitive devices are advantageous owing to their simple structures and high reliability[73–75].

Various strategies for enhancing their sensitivity and pressure detection range have also been developed. The most widely adopted methods use microstructured dielectric layers, such as micropyramid arrays and porous dielectric layers[75,76] (Fig. 1j). In the micropyramid structure, deformation in the dielectric layer can occur at the tip of the pyramidal shape even at extremely low pressures (even a few pascals, enough for measuring small insects) owing to the concentration of pressure at the tip. In the porous dielectric layer, similarly, pores can be deformed even at low pressure (<10 Pa)[77]. Such geometrical change of the dielectric layer results in changes in the capacitance. However, piezocapacitive-based conformable sensors with microstructured or porous dielectric layers have a limited detection range owing to the saturation of the deformability of the dielectric layer[78].

In iontronic devices, various types of ionic media including ionic liquids, hydrogels and organogels have been utilized[34,79]. The pros and cons of each ionic medium are discussed in Supplementary Note 5. Iontronic devices with microstructured ionic media have both high sensitivity and a wide pressure-sensing range. For instance, hydrogels with intrafillable ionic-medium-based iontronic devices showed extremely high sensitivity (3.3 Pa^{-1}) and high resolution (could sense the removal of 17 kg of load from a car with 2,000 kg weight)[35]. Despite these performances, several limitations including liquid leakage, phase separation and water evaporation need to be overcome[79,80] (Table 2).

Triboelectric devices. To induce large charge separation through the triboelectric effect, two interfacing materials should have a large gap in their triboelectric series[81], such that the device can generate electrical voltage upon mechanical deformation with high sensitivity. For instance, fluoropolymers (polytetrafluoroethylene), polyvinyl chloride, polydimethylsiloxane and polyimide have high electron affinity, indicating that these materials have a high tendency to get electrons from other materials when making contact[82]. By contrast, glass, dry skin, air, nylon and cotton have low electron affinity, indicating that these materials easily lose electrons when in contact with other materials[82]. Hence, it is critical to select appropriate contact materials to obtain highly sensitive sensors.

To effectively convert mechanical signals into electrical signals, changes in contact area should be accompanied by continuous repetitive touching and detaching or sliding motions, which lead to surface charge transfer. Devices with a textured surface or that enable sliding motions can facilitate such charge transfer. Textured surfaces can be fabricated through various methods, including the growth of vertical nanowire arrays[83,84], reactive ion etching[85], micropattern moulding[86,87] and the weaving of fabric materials[88]. Triboelectricity-based external biomechanics sensors can be designed to be highly biocompatible, conformable and sensitive, but the triboelectric effect is highly sensitive to moisture. Triboelectric materials are also prone to degradation by mechanical fatigue (Table 2).

Piezoelectronic devices. Piezoelectric materials can be divided into two categories: inorganic ceramics and organic materials. Inorganic piezoelectric materials include lead–zirconate–titanate ($Pb(Zr_{1-x}Ti_x)O_3$, PZT)-based, $PbMg_{1/3}Nb_{2/3}O_3$-$PbTiO_3$ (PMN-PT)-based, $BaTiO_3$, $K_{1/2}Na_{1/2}NbO_3$ (KNN), ZnO, GaN and AlN[89]. Inorganic ceramic piezoelectric materials possess good piezoelectric properties, such as a high electromechanical coupling coefficient, which denotes the effectiveness of the transduction between electrical and mechanical energy. However, similar to inorganic semiconducting materials, they are incompatible with conformable devices owing to their inherent brittleness. Hence, similar strategies have been adopted to design conformable inorganic ceramic-based piezoelectronic devices. For instance, adopting serpentine interconnects and placing the PZT film in the NMP can substantially reduce the applied strain to the PZT layer[5]. A PZT layer with such geometry was only subjected to a total strain of 0.1% when bent with a 0.3 mm bending radius. Similar approaches were also applied to other inorganic piezoelectric thin films including AlN and GaN (refs. 90,91).

Several organic materials including polyvinylidene fluoride (PVDF)-based copolymer, poly(L-lactic acid), glycine, silk and cellulose are piezoelectric because they have large permanent dipoles in their polymer chains[92] (Fig. 1k). Although organic piezoelectric materials have lower piezoelectric performance (low electromechanical coupling coefficient) compared with inorganic piezoelectric materials, they have several advantages including relatively easy fabrication through various solution processing methods, high flexibility with low Young's modulus, good biocompatibility, light weight, low dielectric constant and low acoustic impedance[93,94]. Among various fabrication processes, electrospinning is highly effective at forming high-performance organic piezoelectric thin films (Supplementary Note 6).

Most conformable devices for decoding external soft tissues can sense normal stresses such as stretching and pressing. However, it is still challenging for conformable devices to differentiate shear stress from normal stress. To overcome this challenge, novel signal processing and device design have been proposed (Supplementary Note 7).

Decoding internal tissue biomechanics

Internal tissue biomechanics conveys important information about our health (Box 1). To decode signals from internal organs including heart[95], stomach[96] or muscles[97], flexible implantable devices have been suggested. These devices generally use sensing methods that are similar to those used for external tissue biomechanics decoding[98]. However, specific challenges emerge owing to the invasive nature of implantable devices, including power transfer, fast wireless data transmission, biofouling and the necessity of removing the device after use[99,100]. In this regard, various non-invasive methods have also been investigated (Table 3).

To achieve the non-invasive decoding of internal tissue biomechanics, various strategies using tissue-penetrating modalities, such as electromagnetic, acoustic and optical waves, have been adopted (Supplementary Note 8 and Table 3). Among them, ultrasonography, which utilizes high frequency (>20 kHz) acoustic waves, has gained considerable interest because the waves can penetrate deeply through the skin, something that is difficult to achieve using the methods mentioned earlier[101]. By managing the frequency range of the ultrasound wave, the penetration depth can be adjusted[102]. When the penetrated waves interact with deep biological tissues, which have different acoustic characteristics, the reflected waves can provide anatomical information about these tissues in a spatiotemporal manner. Moreover, ultrasonography can harness diverse imaging methods applicable to various objectives (Box 3) and enable the multidimensional (2D and 3D) imaging of internal organs through the judicious design of transducer element arrays[103,104]. Because imaging is an intuitive method to analyse internal tissue biomechanics in real time, it has been effectively adopted in the clinic for internal organ monitoring and tissue anomaly detection, with applications in disease diagnosis and disease progression assessment[105]. Such applications have been realized with conformable ultrasound imaging devices[6,15,106,107].

Table 3 | Comparison of different mechanisms for internal biomechanics decoding

Mechanisms	Sensors	Pros	Cons	Refs.
Ultrasonic methods	Piezoelectric-based transducer stack	Various imaging modes available (A mode, B mode, M mode, Doppler mode) Intuitive imaging (2D, 3D) Deep-depth tissue sensing (~80 mm) Spatial information (wide FOV imaging) Multiplexing element (transmitting–receiving)	Acoustic matching medium (for example, gel) needed Complex circuit and analysis needed	6,15, 106,107
Optical methods	Piezoelectric-based transducer stack (photoacoustic) Photodetector (PPG)	High-dimensional imaging available (photoacoustic) Simple circuit (PPG) Simple decoding (PPG) Compact size (PPG)	Distinct transmitter/receiver pair needed (photoacoustic: laser source-receiver, PPG: light source-photodetector) Shallow depth (photoacoustic: ~30 mm, PPG: ~3 mm) Low-dimensional information (PPG) Limited target tissues (skin and blood vessels) (PPG)	250,252, 262,263
Mechano-acoustic methods	Microphone	Simultaneous decoding of multiple modalities available (heartbeat, respiration, movement, etc.)	Proper attachment site should be adjusted Signal decomposition needed Low-dimensional information	126,264, 265
Electromagnetic methods	Antenna	High spatiotemporal resolution	Noise from antenna deformation Implantable sensing device may be needed	101,251, 266

A mode, amplitude mode; B mode, brightness mode; FOV, field of view; M mode, motion mode; PPG, photoplethysmography.

Ultrasonography using conformable electronic devices

Piezoelectric materials are ideal for transmitting and receiving ultrasound acoustic waves, making them highly suitable for use in ultrasonic transducers for ultrasound imaging[15].

Stack configuration of the ultrasonic transducer. When designing an ultrasonic transducer for ultrasound imaging, a specific stack configuration is necessary to acquire high-resolution images[108] (Fig. 2a). Piezoelectric materials form the core of this stack, enabling the transmission and reception of ultrasound waves. Several crucial parameters including dielectric property, piezoelectric property and acoustic property need to be considered[108,109]. The dielectric permittivity denotes the ability of a material to store electrical energy under electric field, which is related to the polarization and conversion efficiency of the piezoelectric materials. The dielectric permittivity is also related to the electrical impedance of the material, which should be matched with the electrical impedance of the driving electronics to maximize power transmittance, which are connected through the conductive electrode interconnect. For the piezoelectric property, the electromechanical coupling coefficient dictates the effectiveness of the transduction between electrical and mechanical energy. Regarding the acoustic property, the resonant frequency and acoustic impedance reflect the speed of sound in the material, and the acoustic impedance matching between the transducer and the propagating medium is crucial for efficient wave transmission with minimal loss of energy. The matching layer has a crucial role for such acoustic matching, whereas the backing layer attenuates unwanted waves, ensuring that the acoustic energy is focused solely on the target tissue (Supplementary Note 9).

Because ultrasound waves from an optimized device stack can penetrate through tissues with a relatively deeper depth (on the decimetre scale), they are effective for imaging and monitoring configuration and movements of internal deep tissues[101] (Fig. 2b). With proper stack composition design and signal analysis approaches, sub-millimetre resolution can be achieved[101].

Moreover, various modes of imaging can be adopted for diverse purposes, including the amplitude mode (A mode), brightness mode (B mode), motion mode (M mode) and Doppler mode[110] (Box 3).

Conformable single-element ultrasonic transducer. The simplest method to fabricate a conformable ultrasonic transducer is to utilize a single piezoelectric element as the transducer (Fig. 2c) as it can be easily fabricated and is efficient for basic A mode ultrasonography. M mode ultrasonography can be also conducted by integrating consecutive A mode signals[111]. To endow conformability to the device, which is critical for skin contact-based ultrasonography, adopting flexible polymers such as flexible PVDF and PVDF-based polymers as the active piezoelectric material has gained considerable interest[15]. Such polymer-based transducers are highly efficient for measuring skeletal muscle movements[112,113]. However, single-element transducers are limited for 2D imaging as the transducer needs to be spatially translated to capture signals. To enable efficient 2D imaging, an array configuration that incorporates multiple transducer elements is more appropriate.

Rigid array-based ultrasonic transducer with conformable medium. The most conventional device structure for ultrasound imaging is a rigid single array of ultrasonic transducers. In this device configuration, the transducer array has multiple transmitting and receiving elements. Rigid piezoelectric ceramics are mostly used for the active layer, owing to their high electromechanical coupling coefficients[108]. The critical limitation is the rigidity of the array, which limits conformable integration with soft and curved skin surfaces. One approach to enable conformable contact uses curved scaffolds (Fig. 2d). For instance, a nature-inspired honeycomb scaffold enabled the conformable contact of the array to the soft and curved breast tissue[6]. Adopting soft materials as conformable media is another promising potential approach.

Among the soft materials studied, soft bioadhesive hydrogels demonstrated their versatility for internal tissue imaging of various internal organs including heart, lung and stomach[114].

Flexible and stretchable array-based ultrasonic transducer. Efforts to develop arrays that are flexible and stretchable have also been pursued (Fig. 2e). The simplest approach to achieve a flexible array involves integrating rigid elements with flexible substrates and interconnects. Flexible printed circuit boards or other polymer materials can be used as flexible substrates[115]. Beyond flexibility, stretchability is one of the core requirements to enable advanced wearable electronics, ensuring good conformable contact and stable operation of the devices even under dynamic movement[116,117]. In this context, an island–bridge structure, similar to the serpentine island–bridge structure used to fabricate inorganic thin film-based stretchable devices, can be incorporated into the ultrasonic transducer array[118–120].

Another effective approach involves integrating multiple rigid phased arrays with soft, stretchable polymer substrates[106]. This approach enables high-resolution imaging, facilitates the capture of a large field of view and allows the placement of the phased arrays in multiple directions for multidirectional imaging. For flexible and stretchable ultrasonic transducer arrays, accurately identifying the relative position of each element is critical for focusing the beam and for obtaining high-resolution images. Because the relative position of each element can shift owing to skin dynamics, researchers have implemented beam steering techniques based on surface curvature data acquired from additional biomechanics sensors[121] or have employed long wavelength ultrasonography, which is less sensitive to changes in element positioning[122].

Data analysis techniques for device-decoded tissue biomechanics

Data analysis methods, from conventional signal processing to machine-learning models, facilitate the analysis of data obtained from conformable devices[123]. Sensor fusion – the gathering of multidimensional data from various wearable sensors concurrently – is another approach that can enable effective data acquisition and learning for various applications[123].

Conventional signal analysis techniques

Traditional signal analysis techniques are still widely used for data pre-processing and simple data analysis. The most rudimentary but efficient method is signal filtering based on a frequency bandwidth of interest (Fig. 3a). For example, a low pass filter can get rid of high frequency noise, and a high pass filter can attenuate noises from motion

Box 3 | Modes of ultrasound imaging

Ultrasound imaging can harness various types of imaging modes, all of which have different objectives (see the figure).

A mode (amplitude mode) is a simple and basic approach for measuring 1D deformations in internal tissues[283], which depend on the variance of the reflected amplitude after the penetrated wave interacts with the tissue.

B mode (brightness mode) is the most popular mode of ultrasound imaging, especially for medical purposes, because it offers high-resolution and real-time spatial imaging[284]. B mode uses an array of ultrasonic transducers to formulate 2D images from the received amplitudes[284]. In this modality, the amplitudes of the reflected ultrasound waves from each element are converted to grayscale and aligned as a vertical column, and columns from the array elements are concatenated to form a 2D ultrasound image of the internal tissue.

M mode (motion mode) targets a specific direction in the internal tissue[285], which is useful for decoding the temporal biomechanics of the movement of the tissue, for example, during the study of cardiological behaviours. M mode uses the 1D grayscale values obtained from a B mode image, focusing on a specific direction towards the target object. The amplitude values along this direction become a single column in the M mode image, and values acquired at each time step are continuously concatenated as a new column. The method is particularly effective for analysing the biomechanics of localized target areas over time. In an M mode image, the *x* axis represents time, whereas a B mode image captures a single moment in time.

Finally, Doppler mode is based on the Doppler effect[283]. When a transmitted wave is reflected by a moving object, the decoded frequency of the reflected wave changes according to the velocity of the object. The Doppler mode can be used for analysing the intracardiac status with the velocity visualization of the blood in different organs[286,287].

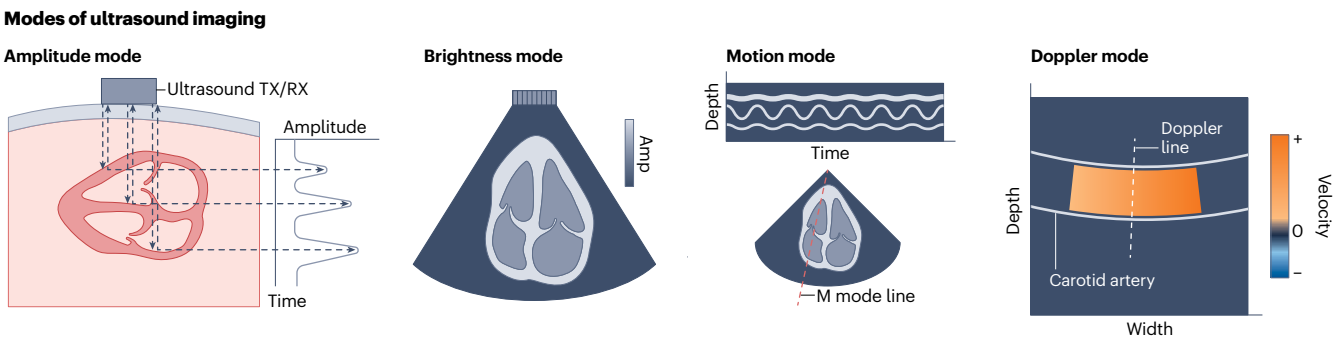

RX, receiver; TX, transmitter.

artefacts that have low frequencies. Moreover, band pass filtering enables the acquisition of signals only within a target bandwidth, which is effective for heartbeat or respiration monitoring as both have typical frequency ranges (heartbeat: 0.9–3 Hz and breath: 0.1–0.7 Hz)[124]. A notch filter can suppress signals from specific frequencies, for example, noises from peripheral electrical devices or power sources.

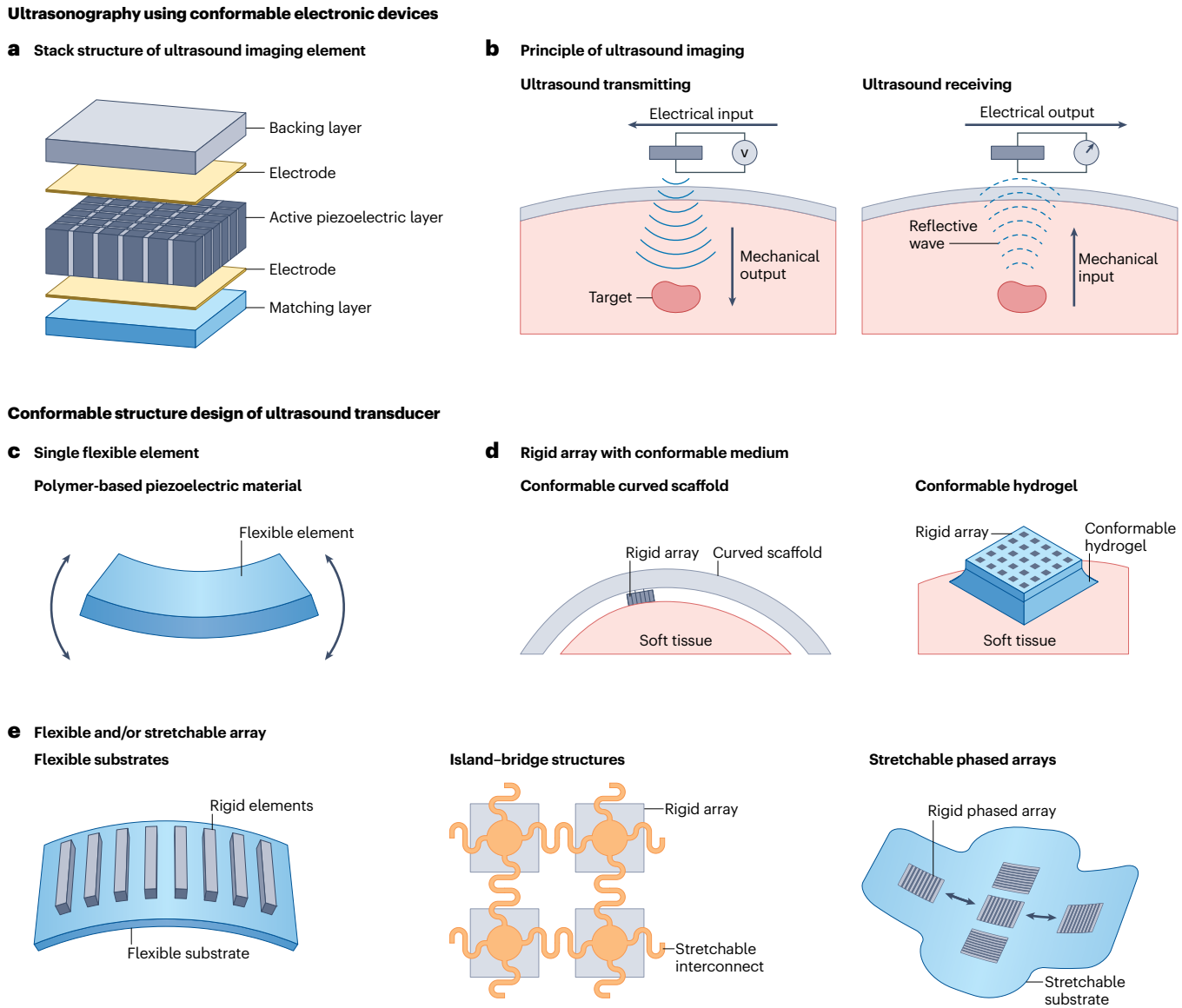

Fig. 2 | Decoding internal tissue biomechanics via conformable ultrasound devices. a, Basic stack structure of the ultrasound imaging element. A matching layer and a backing layer are adopted to achieve high imaging performance. **b**, Basic principle of ultrasound imaging for internal tissue biomechanics decoding. Left: ultrasound transmission. When an electrical input is applied to the piezoelectric active material, mechanical deformation is induced and ultrasound waves are generated from the active layer. The wave can penetrate into the soft tissue, enabling the investigation of deep internal tissue biomechanics. Right: ultrasound receiving. Ultrasound waves reflected from the deep tissue can induce the mechanical deformation of the active piezoelectric material. As different internal tissue layers have distinctive acoustic characteristics, the movement and characteristics of the tissue can be clarified in that the receiver material enables the transduction of the reflected waves into electrical signals. **c**, Single flexible element. A single ultrasound imaging stack can be utilized as an element for ultrasonography. A mode can be operated with a single element, and flexible polymer piezoelectric material, including PVDF-based materials, can be harnessed to render it conformable. **d**, Rigid arrays with conformable medium. Adopting a flexible medium to fabricate conformable ultrasound imaging devices is easy and effective strategy to avoid mechanical mismatch between soft tissue and the rigid stack while preserving the high performance of the rigid piezoelectric material. Conformable curved scaffold (left) and hydrogel (right) allow imaging from the rigid ultrasonic transducer on various curved surfaces. **e**, Flexible and/or stretchable arrays. For a better integration of the device with the skin under dynamic conditions, various flexible designs including using flexible substrates with multiple transducer elements (left), harnessing stretchable interconnects in an island–bridge structure (middle) and using phased arrays with stretchable substrates (right) have been introduced. Panel **e** (middle) adapted with permission from ref. 119, AAAS. Panel **e** (right) adapted from ref. 106, Springer Nature Limited.

Time–frequency domain analysis, including fast Fourier transform (FFT), has been used for the analysis of superimposed biomechanics signals[125] (Fig. 3a). For example, mechano-acoustic signals are usually superimposed with various acoustic signals including heartbeat, respiration, body movement and intestinal sounds[126]. These signals, having different frequencies, can be decomposed using FFT. Statistical methods including linear regression and logistic regression were also used in different demonstrations, such as for the estimation of the exhale volume from the strain measured on the chest[127] and for recognizing sitting posture from pressure sensing on the hip[128].

Machine-learning-aided analysis

In addition to conventional signal analysis techniques, machine-learning methods have been leveraged to enhance data analysis[129,130] (Table 4). To ensure efficient and accurate analysis from machine-learning models, diverse aspects of the collected data and the particularities of the learning process of each model must be considered[131].

Classic machine learning. Classic machine-learning methods[132] can be divided into unsupervised and supervised learning. The main difference between these two learning approaches is the existence of class labels. When handling data without class labels, the data can be categorized according to their characteristics and features. One of the basic unsupervised learning models is principal component analysis (PCA). PCA diminishes the number of variables in the data by adopting orthogonal coordinates called principal components, so that it can selectively secure components having high variances, which typically possess important features and discard components with low variances generally dominant with noises[133]. Because the feature reduction approach using PCA is effective at diminishing noises from biomechanical data and decreases computational costs, it has been efficiently utilized as a preprocessing tool for wearable electronics data[134–136].

K-means clustering is another unsupervised learning model that has been widely used for label-less data clustering. It assigns a predefined number of centres, or clusters (K), and calculates the distance between each data point and these centres. The distance metric can be selected for each case depending on data, with Euclidean distance being the most commonly used[137]. After this calculation, the position of each centre is reassigned according to the calculated means of the distances, and data close to each centre can be clustered without label[137]. *K*-means clustering is efficient for handling large-sized data, but a known number of categories or classes and the initial position of the centroids are needed for high classification accuracy, which generally requires domain knowledge[138]. t-distributed stochastic neighbour embedding (t-SNE) enables the visualization of data with multiple features by converting them into simple 2D or 3D domains using probability distributions[139]. This method is effective for managing nonlinear data, but it requires a high computational cost. Therefore, it has been usually utilized for data visualization[140] or data preprocessing[141] and combined with other machine-learning models.

When class information for each data is provided, it can be utilized as a label to train machine-learning models. Such an approach is called supervised learning. For example, support vector machines (SVMs) generate a hyperplane – a decision boundary that separates classes – with the aim of maximizing the distance between the plane and each data point[142]. This approach allows efficient data classification without incurring high computational costs. *K*-nearest neighbour, another supervised learning approach, is similar to *K*-means clustering, but a label is given to each data point to conduct classification[143]. For new data points, the distances from these data points and the predetermined K number of the nearest existing data points are used for the classification. The final classification result is determined according to the most frequent label among the compared data. SVM and *K*-nearest neighbour models are especially efficient for the analysis of data sets with a small number of labels[18]. Thus, they were used for classifying simple body gestures acquired from various external biomechanics data including pressure and strain[18,90,144]. Random forest is composed of many decision trees with randomly selected data as an ensemble model[145]. A decision tree uses internal attribute tests to guide input data towards a certain decision, and an ensemble of decision trees combines the decisions from multiple trees to generate a final decision (Fig. 3a). Because each tree enables parallelization and subsampling of the data, which reduces the complexity of the model, this method has been efficiently adopted for handling large-sized data[146–148].

Deep learning. Deep-learning models, utilizing neural networks as their backbone[149], also have considerable potential for the analysis of tissue biomechanics data. The basic component of deep learning is a perceptron[150] (Fig. 3a), which can be expressed as[17]:

$$O_j = \sigma(\sum_i w_{ij} X_i + b_j) \quad (4)$$

in which w is the connection weight, b the bias of the node, σ the activation function, X the input data and O the output data. The connection weight denotes the importance of each connection, which critically influences the performance of the model, and b is a parameter that allows a better fit of the model to the data, which are adjustable through learning. The activation function determines the activation of each neuron, which endows nonlinearity to the model for the efficient solving of complex problems. The most rudimentary model of deep learning is the multilayer perceptron, which connects multiple perceptrons[150]. This model has been used for diverse data classification and regression tasks, including the classification of posture for health monitoring from pressure sensor data[17,151]. Although multilayer perceptron is efficient for simple learning from small-sized data[151,152], it is computationally inefficient for large-sized data as each node of the perceptron is connected with each other.

Convolutional neural networks (CNNs) are more computationally efficient for handling of complicated and large-sized data[153]. CNN-based models apply convolutional filters to 2D input data[154] including images[118] and 2D inputs concatenated from multiple 1D data[25]. As CNN harnesses convolution filters[155] and pooling layers (which reduces the spatial dimension of the input for efficient calculation, endowing the model with robustness against transient invariance)[156] for the training, the number of parameters that need to be trained drastically reduces. Hence, the CNN model can handle high-dimensional data, including 2D images and multichannel time-series data (for example, including ultrasound images and mechanical sensor-based motion data), with a relatively low computational cost (Table 4).

Another notable deep-learning model is the recurrent neural network (RNN). One of the advantages of RNN is its ability to consider time variance during computation[157]. RNN uses a hidden state h for one of its inputs, which contains past information as follows[17]:

$$h_t = \sigma(w_f * [h_{t-1}, x_t] + b_f) \quad (5)$$

in which σ is the activation function, x the input data, w the weight and b the bias. As the tissue biomechanics data collected from conformable

Data analysis framework of conformable biomechanics decoding devices

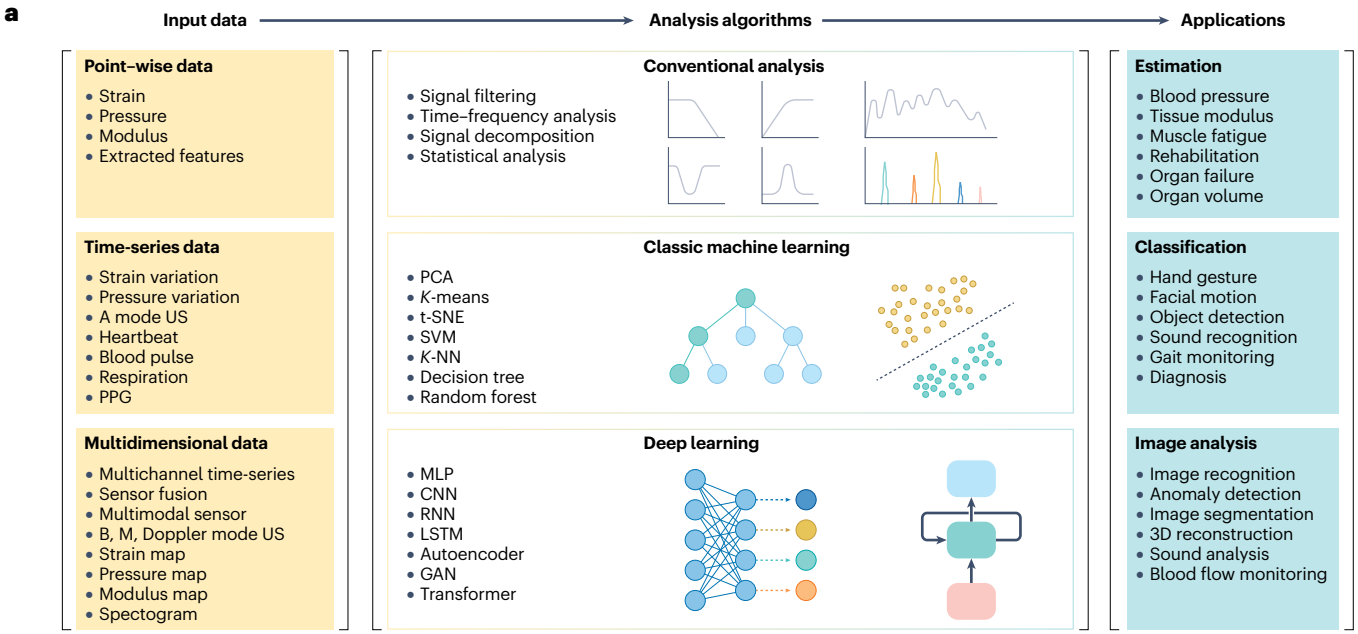

Sensor fusion technology with decoded biomechanical information

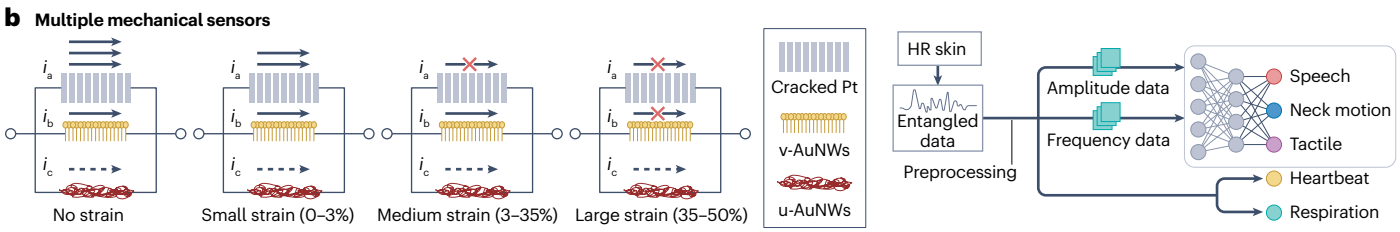

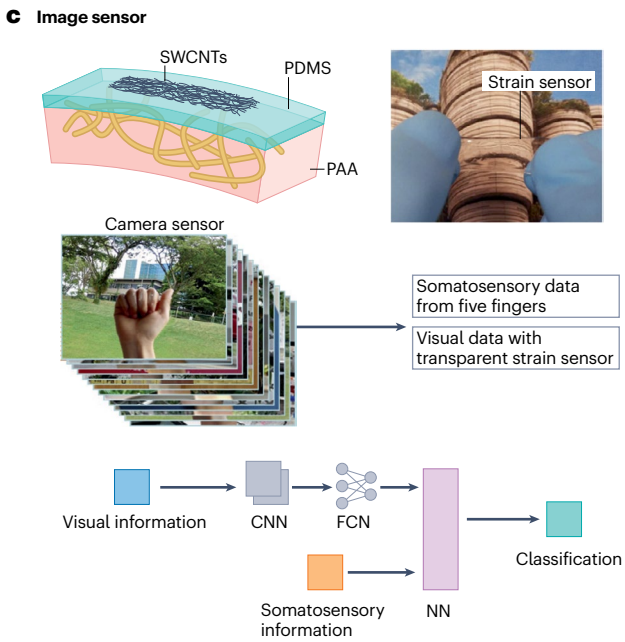

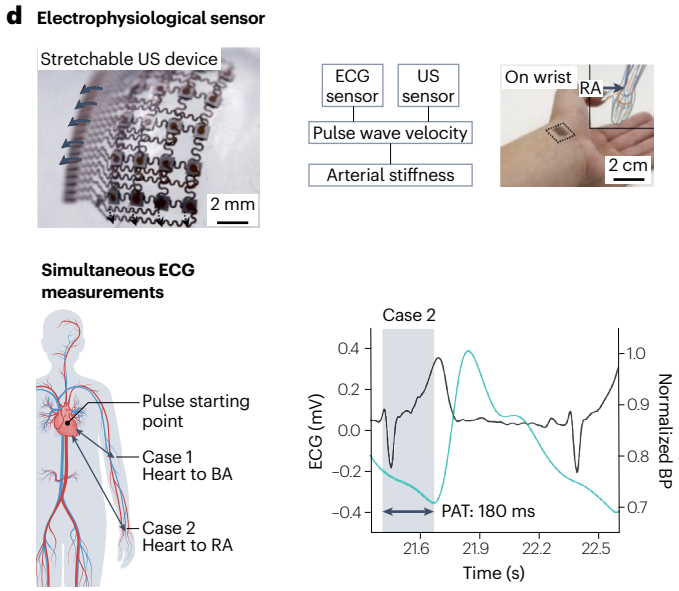

Fig. 3 | Algorithms for soft tissue biomechanics decoding and sensor fusion approaches. a, Overview of the data analysis framework. Input tissue biomechanics data have different dimensionalities that can be analysed with different models including conventional signal analysis techniques, classic machine-learning and deep-learning models. Possible applications include estimation, classification and image analysis. **b**, Multiple mechanical sensor-based fusion. Harnessing multiple mechanical sensors with different sensitivities and sensing range can decode complex information simultaneously (left). For example, by utilizing decoded entangled data, five different biomechanic information can be analysed with a deep-learning approach (right). **c**, Image sensor-based sensor fusion. Somatosensory strain data from a flexible sensor are incorporated with image data of the motion (top). Strain-based somatosensory data and visual image data are collected for the fusion data set (middle). Strain and visual data fusion allows more robust classification of the hand motion with deep-learning approach under various illumination conditions (bottom). **d**, Electrophysiological sensor-based fusion. Merging data from electrophysiological sensors including electrocardiography (ECG) with biomechanics data acquired by stretchable ultrasound (US) device has enabled estimating characteristics of the deep tissue without direct measurement (top). By incorporating the position of the sensors and the time delay between signals from the sensors, pulse wave velocity can be calculated from the pulse arrival time (PAT) at radial artery (RA) (bottom). BA, brachial artery; BP, blood pressure; CNN, convolutional neural network; FCN, fully connected neural network; GAN, generative adversarial network; HR skin, hierarchically resistive skin; LSTM, long short-term memory; NN, neural network; PAA, poly(acrylic acid); PDMS, polydimethylsiloxane; SV data set: somatosensory-visual data set; SWCNT, single-walled carbon nanotube; u-AuNW, ultrathin Au nanowire; v-AuNW, vertically aligned Au nanowire. Panel **b** reprinted from ref. 181, Springer Nature Limited. Panel **c** reprinted from ref. 174, Springer Nature Limited. Panel **d** reprinted from ref. 183, Springer Nature Limited.

devices usually have a temporal component, RNN-based models can be one of the most effective deep-learning models for analysis[158].

Other advanced models, such as long short-term memory[159], autoencoder[160], generative adversarial network[161] and transformer[162], which are based on the models mentioned earlier, have also been used for the analysis of tissue biomechanics data obtained from conformable decoding devices. These models have been applied in various contexts, such as decoding strain information from finger joints for hand movement analysis, sensing pressure on the wrist for hand rehabilitation and predicting missing strain information for tactile perception.

Model selection considering data dimensionality. Input biomechanics data can have varying dimensionality, which can affect the selection of the analysis model. Point-wise data are low-dimensional data that are decoded from intermittent points of time or from a small number of sensor nodes. For example, point-wise values of strain, pressure and skin modulus can be utilized for health monitoring and motion recognition[5,163,164]. Moreover, features, such as amplitude, frequency and statistical features, extracted from complicated data are also valuable point-wise data for efficient computation[144,165]. As these data sets have low dimensionality, simple analysis methods can be applied. For example, collected point-wise strain or pressure data can be clustered using unsupervised machine-learning models such as *K*-means clustering[166] and or simple deep-learning models such as CNN[167] for efficient motion classification. When labelled data are available, supervised learning models such as SVM[144,164] and random forest[164] can be used.

Time-series data are the most common type of tissue biomechanics data and are collected over a certain period of time. Strain variation, pressure variation, A mode ultrasound, heartbeat, respiration, blood pulse and photoplethysmography signals are representative time-series tissue biomechanics data. Conventional signal analysis methods can be used for signal preprocessing and decomposition, and PCA and t-SNE enable dimension reduction for efficient data analysis. Both classic machine-learning and deep-learning methods have been investigated for various estimation and classification applications (Table 4). Among different deep-learning models, RNN-based models can incorporate chronic information by using hidden states for the analysis, and they have been effectively utilized for the analysis of time-series data[158,168,169]. Furthermore, wireless communication[170,171] and on-device learning[172,173], which can enable portable operation by direct learning and decision-making without relying on centralized infrastructures, are relatively easier to be adopted for handling point-wise and time-series data owing to their lower computational cost compared with processing multidimensional image data.

Multidimensional biomechanics data acquisition can be performed using advanced imaging methods and multisensor decoding technology. For example, multichannel time series data[159], sensor fusion data from multiple sensors[174], multimodal data decoded from a single device[175], ultrasound images of organs[118], mapped data of biomechanics modalities[176] and acoustic spectrograms[177] have been analysed with various learning models. Deep-learning models including CNN-based models have been used for image classification[178] and spectrogram analysis[177] for vocal-less voice recognition, which have enabled the efficient monitoring of patients recovering from laryngectomy, even under dynamic motion. Image recognition and segmentation have also been used for cardiovascular status monitoring, enabling the estimation of organ volumes and the tracking of their dynamics[118]. Moreover, combining high-dimensional data from conformable devices — such as 3D reconstructions of muscle ultrasound images[179], volumetric Doppler images of brain blood vessels[107] and volume estimations from 2D images of the bladder and heart[106,118] — with multidimensional analysis methods is expected to enable considerable advances in various applications. However, despite important advancements in analysis techniques for multidimensional input data, wireless communication[178] or on-device learning[140,180] is still limited because of the considerable cost of data transmission and the excessive number of parameters needed in the model for learning.

Sensor fusion strategies

Sensor fusion utilizes multiple sensors to collect multidimensional data synchronously. Advancement in data analysis techniques, such as machine learning, have begun to unlock the potential of the informative, high-dimensional data collected through sensor fusion within conformable devices (Supplementary Note 10).

Sensor fusion for external biomechanics decoding. The sensor fusion strategy involves combining the data from multiple biomechanics sensors having different degrees of sensitivity to increase the sensing range, which is generally limited with a single sensor. For instance, conformable hierarchical wearable sensors composed of multiple strain sensors can use different materials for each sensor layer

Table 4 | Examples of biomechanics decoding using conformable electronic devices combined with data analysis algorithms

Categories	Application	Decoded biomechanics	Decoding method	ML approach	Result
Health monitoring	Continuous pulse wave monitoring with artery detection	Ultrasound on neck	Ultrasound M mode	CNN-based model	98.4% accuracy for ideal and compromised 460 images[178]
	Cardiac state monitoring, organ volume estimation with heart image segmentation	Ultrasound on chest	Ultrasound B mode	CNN-based model	96.01% (axial) and 95.90% (lateral) accuracy for location detection[118]
	Seating posture monitoring	Pressure under hip	Piezoelectric pressure sensor	Random forest	96.7% (random forest) accuracy for 6 postures[267]
Disease classification	Arterial fibrillation	Pressure on wrist	Capacitive pressure sensor	*K*-means clustering	100% accuracy for healthy people (n=13) and patients (n=7)[166]
	Respiratory disease	Pressure on chest	Triboelectric pressure sensor	t-SNE, CNN	99.43% accuracy for 6 diseases[268]
	Lumbar degenerative disease	Pressure on sole of the foot	Piezoelectric pressure sensor	SVM	100% accuracy for healthy people (n=10) and patients (n=10)[144]
Robotics	Quadruped robot control	Strain of fingers	Piezoresistive strain sensor	CNN-based model	96.7% accuracy for 10 motions in the dark situation[174]
	Assistive robot control	Ultrasound on lateral gastrocnemius muscle	Ultrasound B mode	CNN	95.8% (23 out of 24) cases exhibited <10% N-RMSE for plantar flexion moment prediction[186]
	Underwater robot hand control	Strain of fingers	Crack-based strain sensor	MLP	98.1% accuracy for 20 gestures[152]
Communication	Sign-to-speech translation	Strain of each finger	Triboelectric strain sensor	SVM, PCA	98.63% accuracy for 11 gestures[134]
	Facial motion detection	Strain on face	Piezoelectric strain sensor	*K*-NN	86.8% (healthy people) and 75.0% (patients with ALS) for 3 motions[90]
	Mouth motion recognition	Strain on face	Piezoresistive strain sensor	CNN	87.53% accuracy for 100 words[25]
	Vocal-less communication	Strain on neck	Piezoresistive strain sensor	t-SNE, CNN-based model, SVM	99.05% (5 phonemes, 4 tones, 6 words from healthy people), 91% (6 sentences from patients with laryngectomy)[177]
Human–machine interface	Full body motion visualization	Strain of multiple body parts	Crack-based strain sensor	CNN	100% accuracy for 6 motions[140]
	Hand motion classification	Strain on wrist	Crack-based strain sensor	LSTM	96.2% accuracy for 5 motions[158]
	Motion-based keyboard typing and object detection	Strain on finger	Percolation-based strain sensor	Transformer	93.1% accuracy for 26 keypads[162]

ALS, amyotrophic lateral sclerosis; B mode, brightness mode; CNN, convolutional neural network; *K*-NN, *K*-nearest neighbour; LSTM, long short-term memory; M mode, motion mode; ML, machine learning; MLP, multilayer perceptron; N-RMSE, normalized root mean square error; PCA, principal component analysis; SVM, support vector machine; t-SNE, t-distributed stochastic neighbour embedding.

to achieve this goal[181]. If these sensors are connected in parallel, the overall resistance change can reflect data from the different sensing layers. The collected biomechanics data can be decoded from a unified and multilayered sensing device using machine-learning models, and this strategy was used for the recognition of neck motion, heartbeat, breathing and touches to the neck[181] (Fig. 3b).

Tissue biomechanics data also can be efficiently integrated with image-based data (Fig. 3c). For example, the accuracy of hand motion recognition was improved by combining vision-based gesture recognition and tissue biomechanics data[174]. Such data fusion architecture can use pretrained image classification models, which can reduce training time, address data shortage, enhance performance and enable transfer learning by modifying the pretrained model[182]. The output from the pretrained image classification model can then be merged with strain data for the final classification.

Sensor fusion for internal biomechanics decoding. Sensor fusion is also highly effective at internal tissue biomechanics decoding. For example, pulse wave velocity can be calculated by simultaneously recording electrocardiography signals and blood pressure measured through A mode ultrasonography[183] (Fig. 3d). The pulse wave velocity can be calculated as the physical distance between the electrocardiography sensor and the ultrasound device over the pulse arrival time, which is helpful to estimate arterial stiffness.

Combining B mode ultrasound imaging data with other sensory data has also gained considerable attention[184]. Especially, integrating B

mode ultrasound imaging of muscles with surface EMG data obtained from the ambulation analysis is promising for neuromuscular monitoring[185,186]. Sensor fusion achieves superior classification accuracy compared with approaches that leverage single data sets from either B mode ultrasound imaging or surface EMG[185].

Applications

Advancements in conformable devices for decoding external and internal tissue biomechanics rely on advanced materials, structural designs and data-driven approaches to improve their functionality. By integrating sophisticated machine-learning algorithms and sensor fusion techniques, these devices are capable of capturing and analysing biomechanical data with remarkable precision, paving the way for new applications in medical diagnostics, rehabilitation and wearable technologies.

Applications of external tissue biomechanics decoding

The development of non-invasive conformable methods for decoding external tissue biomechanics, combined with sensor fusion and machine-learning techniques, has enabled a broad range of applications. These applications span from daily health-care monitoring, rehabilitation and diagnostics to human–machine interfaces, including prosthetics, exoskeleton control and AR and VR systems.

Motion detection. One of the most promising applications of external tissue biomechanics decoding is the detection of body motion, including the motion of various joints such as finger, wrist, elbow, shoulder, knee, ankle, neck and back[187–189] (Box 1). Body motion detection can be applied in multiple fields including health care, AR and VR and robotics[20,190]. For instance, joint injuries such as spine fatigue can be alleviated by using motion detection devices[191,192]. Motion detection can also be used to gain insights into diseases such as Parkinson disease through the monitoring of gait motion[193,194]. In AR and VR technology, sensitive body motion detection can reduce discomfort and improve the connection between the real and virtual worlds[195–197]. Devices can be directly attached to the joints or to adjacent muscles that control the joints. Devices conformably attached to the joints (for direct detection of joint movements) should be highly stretchable as the deformation range of the joints is very large (around 135°, 140°, 130° and 100° for knee, elbow, wrist and fingers, respectively)[198,199]. For this purpose, nanomaterials with high aspect ratio (1D and 2D), composites or fibre-based piezoresistive and triboelectric devices have been utilized[200–204]. Similar to EMG, conformable biomechanics sensors can also monitor muscle deformation to track joint motion, but highly sensitive devices utilizing piezoresistive, iontronic, triboelectric and piezoelectric mechanisms are required for this purpose[204–208].

Cardiac and lung activities monitoring. Although the heart and lungs are internal organs, their dynamic activities induce the mechanical deformation of the external skin. By measuring this deformation, cardiac activities such as heart rate, breathing rate and blood pressure can be monitored[16,209] (Fig. 4a). Lung activity causes the continuous movement of the rib cage and airflow from the nasal area and the mouth. Hence, various information including respiration rate, breathing pattern and lung volume can be monitored to diagnose chronic respiratory and infectious diseases[210]. To monitor such lung activities, wearable strain sensors with piezoresistive mechanisms can be attached to the rib cage and abdomen to measure the expansion and contraction of the torso[127]. After calibration, the lung volume and respiration rate can be correlated with the resistance change of the piezoresistive sensor attached to the rib cage[127]. Various sensing mechanisms including piezoelectric, triboelectric, piezocapacitive and piezoresistive effects can be used to measure airflow and verbal activities including respiration rate, coughing and speaking[211–213]. As an example, airflow patterns collected from external biomechanics sensors and analysed using a decision tree algorithm could be used to identify various chronic respiratory diseases including asthma, bronchitis and chronic obstructive pulmonary disease[213].

Because skin deformation induced by cardiac activity is extremely weak (about 4 Pa for peak incident pulse wave observed from the wrist pulse)[214,215], a highly sensitive strain or pressure sensor is required[16,209]. Architectures developed to improve the sensitivity of pulse measurement systems include Si nanostructures, microstructured triboelectric sensors, thin piezoelectric pressure sensor arrays and microcrack-based strain sensors[54,86,215,216]. In addition, as blood pressure calculations based on pulse waves are challenging, deep-learning algorithms have been adopted to analyse the data. For example, blood pressure data obtained from a carbonized fabric-based conformable strain sensor array and analysed using a deep-learning algorithm had an accuracy similar to data gathered using the traditional manual cuff method[16].

Speech recognition. Speech is an extremely essential and efficient communication tool for humans. However, speaking can be disrupted by various physical disorders, including disorders in organs responsible for speaking (tongue, lips, jaw, vocal cords and lungs) or neurological diseases (stroke, cerebral palsy, Parkinson disease and dementia)[177], and by environmental noise. Speech recognition can be realized by monitoring various interactions including the vibration of the vocal cord, the movement of the upper esophagus muscle and movements in facial motion[90,177,217] (Fig. 4b).

To collect fruitful insights, the sensor should be highly sensitive and have fast response time. Ideally, devices should have a response time of <10 ms as this is the timescale of facial skin deformation during speech. Such a fast response time was realized by ultrathin piezoresistive Si nanomembranes (around 3.4 μm) and piezoelectric devices[25,90] (around 7 μm). To monitor the vibration of vocal cords, sensors should be able to monitor vibration frequencies up to 1 kHz, which can be realized by nanomaterial-based and microcrack-based piezoresistive and piezocapacitive sensors[177,217,218]. Waveforms of external tissue deformation collected from conformable devices can be analysed for classification tasks with machine-learning models including CNN generally after preprocessing with FFT[90] (Fig. 4b).

Skin modulus measurement. Skin modulus can be used to determine various skin-related diseases including scleroderma, Ehlers–Danlos syndrome, psoriasis, eczema, melanoma and cancer cell development[5]. Devices for measuring the skin modulus are usually composed of two parts: an actuator to generate acoustic waves that propagate through the skin and a sensor to harness acoustic waves coupled with the skin (Fig. 4c panel). The actuator can be an electromagnetic resonator or piezoelectric transducer, and the sensor can be a strain gauge or piezoelectric sensor[4,5]. When the mechanical vibration is generated from the actuator, the generated waves propagate through and interact with the underlying skin. After interaction, the properties of the propagating wave (frequency, phase and velocity) are changed depending on the mechanical properties of the

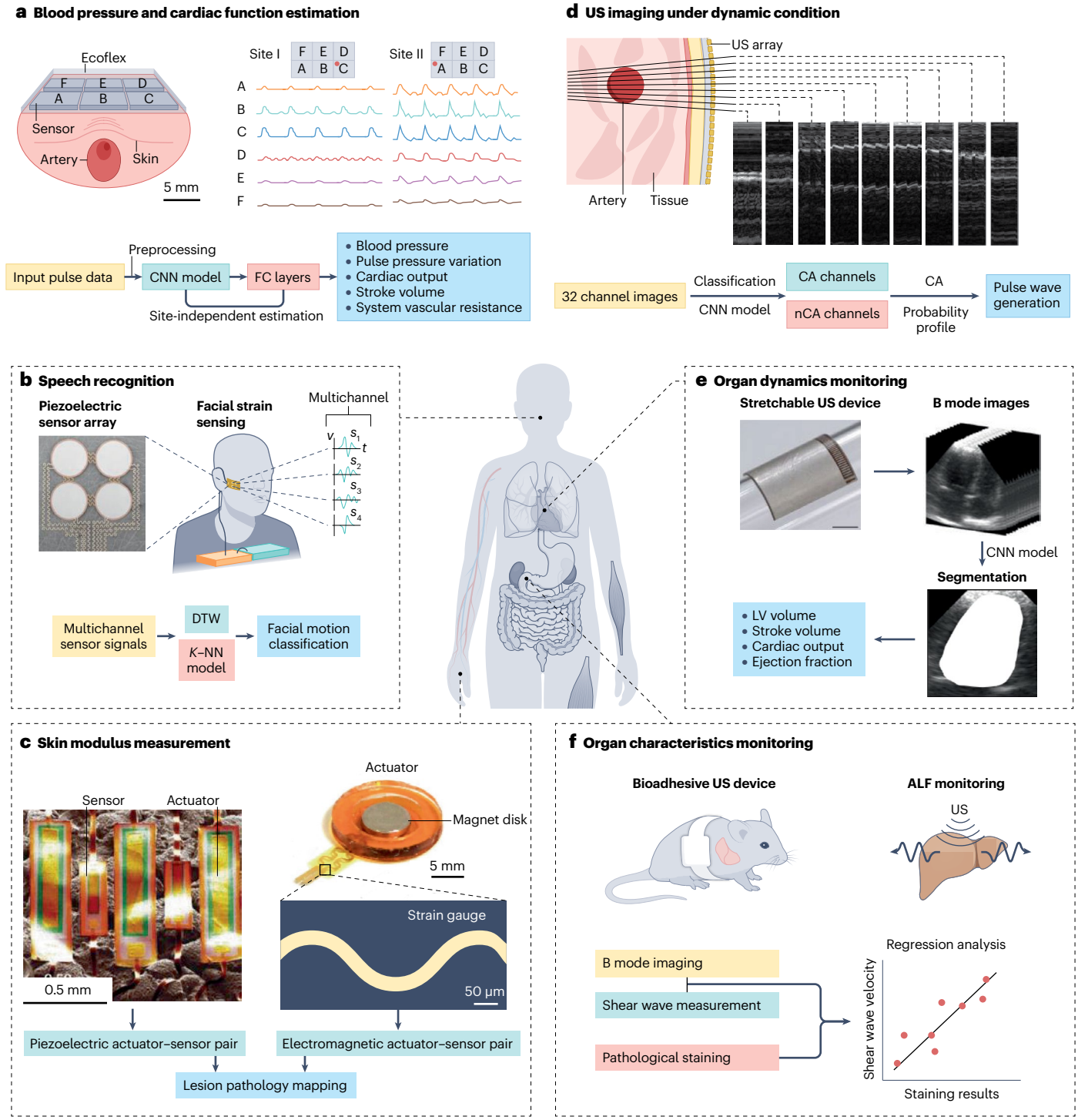

skin[4,5]. This coupled wave can be read from the adjacent conformable devices, and the skin modulus can be calculated by analysing the readout values[4] (Fig. 4c).

Applications of internal tissue biomechanics decoding

For internal tissues, conformable devices can be used for high-resolution imaging in a non-invasive manner. In addition, advanced data analysis techniques including machine learning have enabled efficient and accurate health monitoring and diagnosis.

Organ movement monitoring. The most rudimentary but important application is the monitoring of internal organ movements. The dynamics of various organs including bladder[106], heart[118], diaphragm[114], muscle[179], liver[219] and blood vessels[183] has been successfully decoded

Fig. 4 | Examples of external and internal tissue biomechanics decoding. **a**, Conformable devices for blood pulse wave monitoring. Schematic illustration of the working principle of the device (top left). Decoded waveforms from each sensor channel at different positions on the skin (top right). Preprocessed input data are trained with the convolutional neural network (CNN) model followed by fully connected (FC) layers, which predicts and measures blood pressure, pulse pressure variation, cardiac output, stroke volume and system vascular resistance independent of their position over the artery (bottom). **b**, Conformable devices for speech recognition of a patient with amyotrophic lateral sclerosis (ALS). A photograph of the conformable device attached to the chin of the subject (top left). Schematic illustration of multichannel strain measurements (top right). Decoded multichannel strain data can be trained with dynamic time warping (DTW) and *K*-nearest neighbour (*K*-NN) methods, which enable speech of a patient with ALS (bottom). **c**, Conformable devices for skin modulus measurement. A photograph of a conformable piezoelectric actuator and sensors attached to mock skin (left). Photographs of a conformable electromagnetic actuator and a metal thin film strain gauge. The calculated skin modulus from each sensor enables lesion pathology mapping on skin (right). **d**, Organ movement monitoring with dynamic target detection. Schematic images obtained after utilizing M mode ultrasound (US) images for carotid artery (CA) detection (top). The analysis diagram of CNN model-based classification and pulse wave decoding method (bottom). **e**, Organ movement monitoring with image segmentation. Process diagram of the deep-learning-based image segmentation method operated with stretchable US patch. The CNN model and the principal component analysis method are used to estimate the left ventricular (LV) volume, stroke volume, cardiac output and ejection fraction from the segmented B mode US organ images. **f**, Organ characteristics monitoring for disease monitoring with US devices. Schematics of a wearable bioadhesive US elastography device using acoustic radiation force impulse (ARFI), which enables elastography of the liver to estimate acute liver failure (ALF) progression (top). Pathological staining results and linear regression analysis are used to estimate the mechanical modulus (bottom). nCA, noncarotid artery. Panel **a** reprinted with permission from ref. 16, AAAS. Panel **b** reprinted from ref. 90, Springer Nature Limited. Panel **c** (left) reprinted from ref. 5, Springer Nature Limited. Panel **c** (right) reprinted from ref. 4, Springer Nature Limited. Panel **d** reprinted from ref. 178, Springer Nature Limited. Panel **e** reprinted from ref. 118, Springer Nature Limited. Panel **f** adapted from ref. 219, AAAS.

with ultrasonography from conformable ultrasonic transducers. In detail, organ volume monitoring[106,118], electrophysiological analysis[183], blood volume and velocity analysis[118] have all been successfully demonstrated. Obtaining such biomechanical information from conformable devices can contribute to digital health for daily monitoring, early-stage disease detection and personal care not only in hospitals but also in daily life[220].

In addition, advancements in data analysis have improved the efficiency of conformable ultrasound imaging devices. For example, a conformable ultrasound imaging device was shown to continuously track movements of internal organs by integrating a deep-learning model[178] (Fig. 4d panel), enabling the robust measurement of heart rate and blood pressure even during dynamic exercises[178]. Moreover, organ ultrasound image segmentation with convolution-based deep learning allowed the isolation of data from the target organ from redundant non-target tissues and background noises for more effective analysis[118] (Fig. 4e panel). This approach enabled the calculation of the heart volume variance and cardiac output with an accuracy comparable with conventional imaging techniques.

Organ characteristics monitoring. The mechanical properties of deep tissues are directly related to their physiological states and to disease progression[221]. The formation of abnormalities including tumour and cysts in breast tissues[6] and the progression of muscle tissue's fatigue[179] can be decoded with the ultrasound-based mechanical characteristics analysis. In addition, the stiffness of blood vessels can be estimated by combining biomechanics decoding and electrophysiology monitoring[182]. The 3D elastic modulus mapping of deep muscle tissue was demonstrated using conformable ultrasonic transducer arrays[179]. By integrating images obtained from different steering angles of ultrasound, 2D displacements within deep tissues can be measured and concatenated into 3D images. This approach enables the mapping of the spatial modulus of deep tissues, providing a detailed assessment of their mechanical properties.

Conformable ultrasound devices can also be used to monitor acute liver failure by measuring the modulus of the organ[219] (Fig. 4f). The shear waves induced by acoustic wave in the tissue can be decoded with B mode ultrasound imaging, which helps in evaluating the stiffness of the tissue for elastography. The progression of the disease can then be estimated from the measured elastic modulus of the liver through the linear regression analysis.

Outlook

Soft tissue biomechanics provides some of the most intuitive insights into the physiological processes of the human body. Owing to rapid advancements in materials, device designs and data analysis techniques, the conformable devices have enabled the effective decoding of both external and internal tissue biomechanics on soft tissues. However, important challenges still need to be addressed before these devices can be effectively implemented in real-world applications.

Long-term operation

Many applications of conformable devices require long-term and continuous measurements, but several factors hinder their stability over extended periods of use. First, because most conformable devices are ultrathin, they are vulnerable to mechanical damage during daily activities, which can include external impacts, rubbing or large strains[222]. To address this issue, devices have been protected by additional plastic covers or medical tape, which may limit the operation and flexibility of the device[90,223]. The use of self-healing soft materials, which offer features such as fast healing time (<1 min) and high healing efficiency (almost 100%)[224,225], could be a promising strategy to address this limitation[226]. However, the application of self-healing soft materials to soft tissue biomechanics decoding has not been widely investigated.

Another limitation preventing long-term operation arises from the fact that the device can block sweat glands, which leads to skin inflammation. To mitigate this problem, devices can be designed to allow sweat gland function, either by using porous device structures[227] or by adopting breathable fibre networks or textile substrates[228].

Another important factor that should be considered is the interfacial adhesion between conformable devices and biological tissues. Owing to a mismatch in mechanical properties (Box 2), the contact interface can easily be delaminated, which results in inaccurate sensing and device failure[229,230]. One approach to overcome this limitation is to enhance the interfacial bonding by incorporating functional groups into soft materials that can form strong chemical bonds with biological tissues. For example, chemical moieties with amine groups can strengthen the interface by forming strong covalent bonds with biological tissues[229].

Another strategy is to use thin dry hydrogels that absorb the water on the biological tissues, resulting in strong bonding[229].

Wireless and portable peripheral electronics and their power management

Most studies on conformable devices mainly focus on the sensing component. However, to read electrical values from conformable devices, other electrical components, such as the data acquisition system, should also be optimized. Most conformable devices are connected with external data acquisition systems through wires, which are not feasible for real applications. Hence, peripheral electronics, including data acquisition systems, communication and power management units, should be compact, wearable and allow the receiving and transmission of data wirelessly. Moreover, for the decoding of complicated modalities such as internal tissue biomechanics using ultrasound imaging, advanced chip design using approaches such as field programmable gate arrays is required to handle signal transmission and reception from multiple sensing units[231,232]. Efficient power management is also critical. Although rechargeable batteries can be integrated, strategies that reduce the need for frequent charging are needed. Approaches include the optimization of the data acquisition system components (amplifiers, filters or others)[233], the integration of energy harvesters such as solar cells and nanogenerators[234,235] and the utilization of self-powered sensors with nanogenerators harnessing piezoelectric or triboelectric effect[236]. Wireless power transfer technologies that can charge the batteries using electromagnetic fields or even operate the system without batteries are also promising methods[91,237].

Advanced machine-learning architectures

Current machine-learning algorithms are generally built at the software level. Hence, data are sent to a server for training and inference, which causes latency, data privacy issues and extra power consumption[238]. To alleviate these issues, on-device computing, which downloads the trained weight values or models into portable computing devices, such as smartphones or personal computers, and runs inferences in the portable hardware, is gaining major interest[238]. To achieve on-device computing, novel neuromorphic memristive devices with portable, power-efficient and even conformable neuromorphic computing devices can be effective, as conventional complementary metal-oxide-semiconductor-based neuromorphic hardware requires large components and are not conformable[239–241]. Furthermore, applying model minimization strategies to deep-learning models[242,243] could solve this bottleneck towards the realization of fully portable and learnable conformable tissue biomechanics decoding devices.

Published online: 21 October 2024

References

1. Fung, Y.-C. *Biomechanics: Mechanical Properties of Living Tissues* (Springer, 2013).
2. Libanori, A., Chen, G., Zhao, X., Zhou, Y. & Chen, J. Smart textiles for personalized healthcare. *Nat. Electron.* **5**, 142–156 (2022).
3. Deng, W. et al. Piezoelectric nanogenerators for personalized healthcare. *Chem. Soc. Rev.* **51**, 3380–3435 (2022).
4. Song, E. et al. Miniaturized electromechanical devices for the characterization of the biomechanics of deep tissue. *Nat. Biomed. Eng.* **5**, 759–771 (2021).
5. Dagdeviren, C. et al. Conformal piezoelectric systems for clinical and experimental characterization of soft tissue biomechanics. *Nat. Mater.* **14**, 728–736 (2015).
6. Du, W. et al. Conformable ultrasound breast patch for deep tissue scanning and imaging. *Sci. Adv.* **9**, eadh5325 (2023).
7. Lee, J. et al. Stretchable and suturable fibre sensors for wireless monitoring of connective tissue strain. *Nat. Electron.* **4**, 291–301 (2021).
8. Kwak, S. S., Yoon, H. J. & Kim, S. W. Textile-based triboelectric nanogenerators for self-powered wearable electronics. *Adv. Funct. Mater.* **29**, 1804533 (2019).
9. Heng, W., Solomon, S. & Gao, W. Flexible electronics and devices as human–machine interfaces for medical robotics. *Adv. Mater.* **34**, 2107902 (2022).
10. Luo, Y. et al. Learning human–environment interactions using conformal tactile textiles. *Nat. Electron.* **4**, 193–201 (2021).
11. Kim, H. et al. Recent advances in wearable sensors and integrated functional devices for virtual and augmented reality applications. *Adv. Funct. Mater.* **31**, 2005692 (2021).
12. Chen, G. et al. Electronic textiles for wearable point-of-care systems. *Chem. Rev.* **122**, 3259–3291 (2021).
13. van Netten, J. P., Cann, S. H., Thornton, I. & Finegan, R. Growing concern following compression mammography. *Case Rep.* **2016**, bcr2016216889 (2016).
14. Thomas, T. The urban–rural health divide: technology's role in enhancing rural medicine. *GRC Insights* https://insights.grcglobalgroup.com/the-urban-rural-health-divide-technologys-role-in-enhancing-rural-medicine (2023).
15. Zhang, L., Du, W., Kim, J. H., Yu, C. C. & Dagdeviren, C. An emerging era: conformable ultrasound electronics. *Adv. Mater.* **36**, 2307664 (2024).
16. Li, S. et al. Monitoring blood pressure and cardiac function without positioning via a deep learning-assisted strain sensor array. *Sci. Adv.* **9**, eadh0615 (2023).
17. Qiao, Y. et al. Soft electronics for health monitoring assisted by machine learning. *Nano-Micro Lett.* **15**, 66 (2023).
18. Wang, Y. et al. Machine learning-enhanced flexible mechanical sensing. *Nano-Micro Lett.* **15**, 55 (2023).
19. Wang, B. & Facchetti, A. Mechanically flexible conductors for stretchable and wearable e-skin and e-textile devices. *Adv. Mater.* **31**, 1901408 (2019).
20. Yin, R., Wang, D., Zhao, S., Lou, Z. & Shen, G. Wearable sensors-enabled human–machine interaction systems: from design to application. *Adv. Funct. Mater.* **31**, 2008936 (2021).
21. Zhao, H. et al. A new model based on the in-plane deformation for the conformal piezoelectric systems for characterization of soft tissue modulus. *Extreme Mech. Lett.* **55**, 101801 (2022).
22. Li, F. et al. Recent advances in strain-induced piezoelectric and piezoresistive effect-engineered 2D semiconductors for adaptive electronics and optoelectronics. *Nanomicro Lett.* **12**, 1–44 (2020).
23. Fiorillo, A., Critello, C. & Pullano, S. Theory, technology and applications of piezoresistive sensors: a review. *Sens. Actuators A Phys.* **281**, 156–175 (2018).
24. Welser, J., Hoyt, J., Takagi, S.-I. & Gibbons, J. Strain dependence of the performance enhancement in strained-Si n-MOSFETs. In *Proc. 1994 IEEE Int. Electron Devices Meeting* 373–376 (IEEE, 1994).
25. Kim, T. et al. Ultrathin crystalline-silicon-based strain gauges with deep learning algorithms for silent speech interfaces. *Nat. Commun.* **13**, 5815 (2022).
26. Nguyen, T. et al. Advances in ultrasensitive piezoresistive sensors: from conventional to flexible and stretchable applications. *Mater. Horiz.* **8**, 2123–2150 (2021).
27. Choi, J. et al. Hierarchical 3D percolation network of Ag–Au core–shell nanowire–hydrogel composite for efficient biohybride electrodes. *ACS Nano* **17**, 17966–17978 (2023).
28. Choi, S., Lee, H., Ghaffari, R., Hyeon, T. & Kim, D. H. Recent advances in flexible and stretchable bio-electronic devices integrated with nanomaterials. *Adv. Mater.* **28**, 4203–4218 (2016).
29. Won, D. et al. Transparent electronics for wearable electronics application. *Chem. Rev.* **123**, 9982–10078 (2023).
30. Hu, N., Karube, Y., Yan, C., Masuda, Z. & Fukunaga, H. Tunneling effect in a polymer/carbon nanotube nanocomposite strain sensor. *Acta Mater.* **56**, 2929–2936 (2008).
31. Liu, H. et al. Soft elastomeric capacitor for strain and stress monitoring on sutured skin tissues. *ACS Sens.* **6**, 3706–3714 (2021).
32. Souri, H. et al. Wearable and stretchable strain sensors: materials, sensing mechanisms, and applications. *Adv. Intell. Syst.* **2**, 2000039 (2020).
33. Li, X. et al. Wearable, washable, and highly sensitive piezoresistive pressure sensor based on a 3D sponge network for real-time monitoring human body activities. *ACS Appl. Mater. Interfaces* **13**, 46848–46857 (2021).
34. Ren, Z. et al. Ionic flexible mechanical sensors: mechanisms, structural engineering, applications, and challenges. *Adv. Sens. Res.* **2**, 2200099 (2023).
35. Bai, N. et al. Graded intrafillable architecture-based iontronic pressure sensor with ultra-broad-range high sensitivity. *Nat. Commun.* **11**, 209 (2020).
36. Liu, Z. et al. Wearable and implantable triboelectric nanogenerators. *Adv. Funct. Mater.* **29**, 1808820 (2019).
37. Wang, Z. L. Triboelectric nanogenerators as new energy technology for self-powered systems and as active mechanical and chemical sensors. *ACS Nano* **7**, 9533–9557 (2013).
38. Kim, W.-G. et al. Triboelectric nanogenerator: structure, mechanism, and applications. *ACS Nano* **15**, 258–287 (2021).
39. Lowell, J. & Rose-Innes, A. Contact electrification. *Adv. Phys.* **29**, 947–1023 (1980).
40. Xia, X., Wang, H., Guo, H., Xu, C. & Zi, Y. On the material-dependent charge transfer mechanism of the contact electrification. *Nano Energy* **78**, 105343 (2020).
41. Tat, T., Libanori, A., Au, C., Yau, A. & Chen, J. Advances in triboelectric nanogenerators for biomedical sensing. *Biosens. Bioelectron.* **171**, 112714 (2021).
42. Gao, Q., Cheng, T. & Wang, Z. L. Triboelectric mechanical sensors — progress and prospects. *Extreme Mech. Lett.* **42**, 101100 (2021).
43. Dagdeviren, C. et al. Recent progress in flexible and stretchable piezoelectric devices for mechanical energy harvesting, sensing and actuation. *Extreme Mech. Lett.* **9**, 269–281 (2016).

44. Mo, X. et al. Piezoelectrets for wearable energy harvesters and sensors. *Nano Energy* **65**, 104033 (2019).
45. Hall, D. Review nonlinearity in piezoelectric ceramics. *J. Mater. Sci.* **36**, 4575–4601 (2001).
46. Yu, K. J., Yan, Z., Han, M. & Rogers, J. A. Inorganic semiconducting materials for flexible and stretchable electronics. *npj Flex. Electron.* **1**, 4 (2017).
47. Wang, C., Kinzel, G. & Altan, T. Mathematical modeling of plane-strain bending of sheet and plate. *J. Mater. Process. Technol.* **39**, 279–304 (1993).
48. Gupta, S., Navaraj, W. T., Lorenzelli, L. & Dahiya, R. Ultra-thin chips for high-performance flexible electronics. *npj Flex. Electron.* **2**, 8 (2018).
49. Hu, J. et al. Flexible integrated photonics: where materials, mechanics and optics meet. *Opt. Mater. Express* **3**, 1313–1331 (2013).
50. Won, S. M. et al. Multimodal sensing with a three-dimensional piezoresistive structure. *ACS Nano* **13**, 10972–10979 (2019).
51. Zhang, C., Sun, J., Lu, Y. & Liu, J. Nanocrack-based strain sensors. *J. Mater. Chem. C* **9**, 754–772 (2021).
52. Matsuhisa, N. et al. High-transconductance stretchable transistors achieved by controlled gold microcrack morphology. *Adv. Electron. Mater.* **5**, 1900347 (2019).
53. Zhu, J. et al. Tuning strain sensor performance via programmed thin-film crack evolution. *ACS Appl. Mater. Interfaces* **13**, 38105–38113 (2021).
54. Jiang, Z. et al. A 1.3-micrometre-thick elastic conductor for seamless on-skin and implantable sensors. *Nat. Electron.* **5**, 784–793 (2022).
55. Jheng, W.-W. et al. Gold nanoparticle thin film-based strain sensors for monitoring human pulse. *ACS Appl. Nano Mater.* **4**, 1712–1718 (2021).
56. Huang, C. B. et al. Highly sensitive strain sensors based on molecules–gold nanoparticles networks for high-resolution human pulse analysis. *Small* **17**, 2007593 (2021).
57. Jiang, C.-W., Ni, I.-C., Tzeng, S.-D. & Kuo, W. Nearly isotropic piezoresistive response due to charge detour conduction in nanoparticle thin films. *Sci. Rep.* **5**, 11939 (2015).
58. Segev-Bar, M. & Haick, H. Flexible sensors based on nanoparticles. *ACS Nano* **7**, 8366–8378 (2013).
59. Jung, J. et al. Stretchable/flexible silver nanowire electrodes for energy device applications. *Nanoscale* **11**, 20356–20378 (2019).
60. Gupta, A., Sakthivel, T. & Seal, S. Recent development in 2D materials beyond graphene. *Prog. Mater. Sci.* **73**, 44–126 (2015).
61. Novoselov, K. S., Mishchenko, A., Carvalho, A. & Castro Neto, A. 2D materials and van der Waals heterostructures. *Science* **353**, aac9439 (2016).
62. Mannix, A. J., Kiraly, B., Hersam, M. C. & Guisinger, N. P. Synthesis and chemistry of elemental 2D materials. *Nat. Rev. Chem.* **1**, 0014 (2017).
63. Cai, X., Luo, Y., Liu, B. & Cheng, H.-M. Preparation of 2D material dispersions and their applications. *Chem. Soc. Rev.* **47**, 6224–6266 (2018).
64. Han, S. et al. Fast plasmonic laser nanowelding for a Cu-nanowire percolation network for flexible transparent conductors and stretchable electronics. *Adv. Mater.* **26**, 5808–5814 (2014).
65. Amjadi, M., Pichitpajongkit, A., Lee, S., Ryu, S. & Park, I. Highly stretchable and sensitive strain sensor based on silver nanowire–elastomer nanocomposite. *ACS Nano* **8**, 5154–5163 (2014).
66. Jung, D. et al. Highly conductive and elastic nanomembrane for skin electronics. *Science* **373**, 1022–1026 (2021).
67. Sun, Y., Yin, Y., Mayers, B. T., Herricks, T. & Xia, Y. Uniform silver nanowires synthesis by reducing $AgNO_3$ with ethylene glycol in the presence of seeds and poly (vinyl pyrrolidone). *Chem. Mater.* **14**, 4736–4745 (2002).
68. Zhan, H. et al. Synthesis of silver flakes and their application as conductive filler for low-curing-temperature silver pastes. *J. Electron. Mater.* **48**, 2745–2753 (2019).
69. Yeh, Y.-C., Creran, B. & Rotello, V. M. Gold nanoparticles: preparation, properties, and applications in bionanotechnology. *Nanoscale* **4**, 1871–1880 (2012).
70. Habte, A. T. & Ayele, D. W. Synthesis and characterization of reduced graphene oxide (rGO) started from graphene oxide (GO) using the tour method with different parameters. *Adv. Mater. Sci. Eng.* **2019**, 5058163 (2019).
71. Sun, Y., Gates, B., Mayers, B. & Xia, Y. Crystalline silver nanowires by soft solution processing. *Nano Lett.* **2**, 165–168 (2002).
72. Choi, S. H. et al. Large-scale synthesis of graphene and other 2D materials towards industrialization. *Nat. Commun.* **13**, 1484 (2022).
73. Huang, Y., Fan, X., Chen, S. C. & Zhao, N. Emerging technologies of flexible pressure sensors: materials, modeling, devices, and manufacturing. *Adv. Funct. Mater.* **29**, 1808509 (2019).
74. Ha, K.-H., Huh, H., Li, Z. & Lu, N. Soft capacitive pressure sensors: trends, challenges, and perspectives. *ACS Nano* **16**, 3442–3448 (2022).
75. Nie, Z., Kwak, J. W., Han, M. & Rogers, J. A. Mechanically active materials and devices for bio-interfaced pressure sensors — a review. *Adv. Mater.* https://doi.org/10.1002/adma.202205609 (2022).
76. Mannsfeld, S. C. et al. Highly sensitive flexible pressure sensors with microstructured rubber dielectric layers. *Nat. Mater.* **9**, 859–864 (2010).
77. Kwon, D. et al. Highly sensitive, flexible, and wearable pressure sensor based on a giant piezocapacitive effect of three-dimensional microporous elastomeric dielectric layer. *ACS Appl. Mater. Interfaces* **8**, 16922–16931 (2016).
78. Cui, X. et al. Flexible pressure sensors via engineering microstructures for wearable human–machine interaction and health monitoring applications. *iScience* **25**, 104148 (2022).
79. Choi, S.-G., Kang, S.-H., Lee, J.-Y., Park, J.-H. & Kang, S.-K. Recent advances in wearable iontronic sensors for healthcare applications. *Front. Bioeng. Biotechnol.* **11**, 1335188 (2023).
80. Xiang, S., He, X., Zheng, F. & Lu, Q. Multifunctional flexible sensors based on ionogel composed entirely of ionic liquid with long alkyl chains for enhancing mechanical properties. *Chem. Eng. J.* **439**, 135644 (2022).
81. Zou, H. et al. Quantifying the triboelectric series. *Nat. Commun.* **10**, 1427 (2019).
82. Xiong, X., Liang, J. & Wu, W. Principle and recent progress of triboelectric pressure sensors for wearable applications. *Nano Energy* **113**, 108542 (2023).
83. Park, I. W. et al. Vertically aligned cyclo-phenylalanine peptide nanowire-based high-performance triboelectric energy generator. *Nano Energy* **57**, 737–745 (2019).
84. An, T. et al. Self-powered gold nanowire tattoo triboelectric sensors for soft wearable human–machine interface. *Nano Energy* **77**, 105295 (2020).
85. Yang, J. et al. Eardrum-inspired active sensors for self-powered cardiovascular system characterization and throat-attached anti-interference voice recognition. *Adv. Mater.* **27**, 1316–1326 (2015).
86. Xu, R., Luo, F., Zhu, Z., Li, M. & Chen, B. Flexible wide-range triboelectric sensor for physiological signal monitoring and human motion recognition. *ACS Appl. Electron. Mater.* **4**, 4051–4060 (2022).
87. Fan, F.-R. et al. Transparent triboelectric nanogenerators and self-powered pressure sensors based on micropatterned plastic films. *Nano Lett.* **12**, 3109–3114 (2012).
88. Hu, C., Wang, F., Cui, X. & Zhu, Y. Recent progress in textile-based triboelectric force sensors for wearable electronics. *Adv. Compos. Hybrid Mater.* **6**, 70 (2023).
89. Bowen, C., Kim, H., Weaver, P. & Dunn, S. Piezoelectric and ferroelectric materials and structures for energy harvesting applications. *Energy Environ. Sci.* **7**, 25–44 (2014).
90. Sun, T. et al. Decoding of facial strains via conformable piezoelectric interfaces. *Nat. Biomed. Eng.* **4**, 954–972 (2020).
91. Kim, Y. et al. Chip-less wireless electronic skins by remote epitaxial freestanding compound semiconductors. *Science* **377**, 859–864 (2022).
92. Vijayakanth, T., Liptrot, D. J., Gazit, E., Boomishankar, R. & Bowen, C. R. Recent advances in organic and organic–inorganic hybrid materials for piezoelectric mechanical energy harvesting. *Adv. Funct. Mater.* **32**, 2109492 (2022).
93. Li, L. et al. Recent progress in piezoelectric thin film fabrication via the solvothermal process. *J. Mater. Chem. A* **7**, 16046–16067 (2019).
94. Chen, C. et al. Additive manufacturing of piezoelectric materials. *Adv. Funct. Mater.* **30**, 2005141 (2020).
95. Dual, S. A. et al. Continuous heart volume monitoring by fully implantable soft strain sensor. *Adv. Healthc. Mater.* **9**, 2000855 (2020).
96. Dagdeviren, C. et al. Flexible piezoelectric devices for gastrointestinal motility sensing. *Nat. Biomed. Eng.* **1**, 807–817 (2017).
97. Han, M. et al. Three-dimensional piezoelectric polymer microsystems for vibrational energy harvesting, robotic interfaces and biomedical implants. *Nat. Electron.* **2**, 26–35 (2019).
98. Shen, Z. et al. Progress of flexible strain sensors for physiological signal monitoring. *Biosens. Bioelectron.* **211**, 114298 (2022).
99. Bazaka, K. & Jacob, M. V. Implantable devices: issues and challenges. *Electronics* **2**, 1–34 (2012).
100. Erathodiyil, N., Chan, H.-M., Wu, H. & Ying, J. Y. Zwitterionic polymers and hydrogels for antibiofouling applications in implantable devices. *Mater. Today* **38**, 84–98 (2020).
101. Lin, M., Hu, H., Zhou, S. & Xu, S. Soft wearable devices for deep-tissue sensing. *Nat. Rev. Mater.* **7**, 850–869 (2022).
102. Ng, A. & Swanevelder, J. Resolution in ultrasound imaging. *Continuing Educ. Anaesthesia Crit. Care Pain* **11**, 186–192 (2011).
103. Fenster, A., Downey, D. B. & Cardinal, H. N. Three-dimensional ultrasound imaging. *Phys. Med. Biol.* **46**, R67 (2001).
104. Huang, Q. & Zeng, Z. A review on real-time 3D ultrasound imaging technology. *Biomed Res. Int.* **2017**, 6027029 (2017).
105. Wells, P. N. & Liang, H.-D. Medical ultrasound: imaging of soft tissue strain and elasticity. *J. R. Soc. Interface* **8**, 1521–1549 (2011).
106. Zhang, L. et al. A conformable phased-array ultrasound patch for bladder volume monitoring. *Nat. Electron.* **7**, 77–90 (2024).
107. Zhou, S. et al. Transcranial volumetric imaging using a conformal ultrasound patch. *Nature* **629**, 810–818 (2024).
108. Zhou, Q., Lam, K. H., Zheng, H., Qiu, W. & Shung, K. K. Piezoelectric single crystal ultrasonic transducers for biomedical applications. *Prog. Mater. Sci.* **66**, 87–111 (2014).
109. Yu, C. C. et al. A conformable ultrasound patch for cavitation-enhanced transdermal cosmeceutical delivery. *Adv. Mater.* **35**, 2300066 (2023).
110. Li, Y. et al. Progress in wearable acoustical sensors for diagnostic applications. *Biosens. Bioelectron.* **237**, 115509 (2023).
111. Steinberg, S., Ono, Y., Rajan, S. & Venugopal, S. Continuous artery wall motion tracking using flexible and wearable ultrasonic sensor by signal decomposition. In *IEEE Int. Conf. Flexible Printable Sens. Syst. (FLEPS)* 1–4 (IEEE, 2021).
112. AlMohimeed, I. & Ono, Y. Ultrasound measurement of skeletal muscle contractile parameters using flexible and wearable single-element ultrasonic sensor. *Sensors* **20**, 3616 (2020).
113. Fernandes, A. J., Ono, Y. & Ukwatta, E. Evaluation of finger flexion classification at reduced lateral spatial resolutions of ultrasound. *IEEE Access* **9**, 24105–24118 (2021).
114. Wang, C. et al. Bioadhesive ultrasound for long-term continuous imaging of diverse organs. *Science* **377**, 517–523 (2022).
115. Elloian, J. et al. Flexible ultrasound transceiver array for non-invasive surface-conformable imaging enabled by geometric phase correction. *Sci. Rep.* **12**, 16184 (2022).

116. Lee, J., Llerena Zambrano, B., Woo, J., Yoon, K. & Lee, T. Recent advances in 1D stretchable electrodes and devices for textile and wearable electronics: materials, fabrications, and applications. *Adv. Mater.* **32**, 1902532 (2020).
117. Yang, J. C. et al. Electronic skin: recent progress and future prospects for skin-attachable devices for health monitoring, robotics, and prosthetics. *Adv. Mater.* **31**, 1904765 (2019).
118. Hu, H. et al. A wearable cardiac ultrasound imager. *Nature* **613**, 667–675 (2023).
119. Hu, H. et al. Stretchable ultrasonic transducer arrays for three-dimensional imaging on complex surfaces. *Sci. Adv.* **4**, eaar3979 (2018).
120. Zhang, Y. et al. Experimental and theoretical studies of serpentine microstructures bonded to prestrained elastomers for stretchable electronics. *Adv. Funct. Mater.* **24**, 2028–2037 (2014).
121. Chen, W. et al. Flexible ultrasound transducer with embedded optical shape sensing fiber for biomedical imaging applications. *IEEE Trans. Biomed. Eng.* **70**, 2841–2851 (2023).
122. Wang, C. et al. Continuous monitoring of deep-tissue haemodynamics with stretchable ultrasonic phased arrays. *Nat. Biomed. Eng.* **5**, 749–758 (2021).
123. Lee, J. H., Cho, K. & Kim, J. K. Age of flexible electronics: emerging trends in soft multifunctional sensors. *Adv. Mater.* **36**, e2310505 (2024).
124. Xiao, Y., Lin, J., Boric-Lubecke, O. & Lubecke, M. Frequency-tuning technique for remote detection of heartbeat and respiration using low-power double-sideband transmission in the Ka-band. *IEEE Trans. Microw. Theory Tech.* **54**, 2023–2032 (2006).
125. Liu, Z. et al. A highly sensitive stretchable strain sensor based on multi-functionalized fabric for respiration monitoring and identification. *Chem. Eng. J.* **426**, 130869 (2021).
126. Yoo, J.-Y. et al. Wireless broadband acousto-mechanical sensing system for continuous physiological monitoring. *Nat. Med.* **29**, 3137–3148 (2023).
127. Chu, M. et al. Respiration rate and volume measurements using wearable strain sensors. *npj Digital Med.* **2**, 8 (2019).
128. Ran, X. et al. A portable sitting posture monitoring system based on a pressure sensor array and machine learning. *Sens. Actuators A Phys.* **331**, 112900 (2021).
129. Matthews, J., Kim, J. & Yeo, W. H. Advances in biosignal sensing and signal processing methods with wearable devices. *Anal. Sens.* **3**, e202200062 (2023).
130. Shi, Q. et al. Progress in wearable electronics/photonics — moving toward the era of artificial intelligence and internet of things. *InfoMat* **2**, 1131–1162 (2020).
131. Gholamiangonabadi, D., Kiselov, N. & Grolinger, K. Deep neural networks for human activity recognition with wearable sensors: leave-one-subject-out cross-validation for model selection. *IEEE Access* **8**, 133982–133994 (2020).
132. Faouzi, J. & Colliot, O. Classic machine learning methods. *Mach. Learn. Brain Disord.* **197**, 25–75 (2023).
133. Abdi, H. & Williams, L. J. Principal component analysis. *Wiley Interdiscip. Rev. Comput. Stat.* **2**, 433–459 (2010).
134. Zhou, Z. et al. Sign-to-speech translation using machine-learning-assisted stretchable sensor arrays. *Nat. Electron.* **3**, 571–578 (2020).
135. Wang, T., Zhao, Y. & Wang, Q. A flexible iontronic capacitive sensing array for hand gesture recognition using deep convolutional neural networks. *Soft Robot.* **10**, 443–453 (2023).
136. Zong, X. et al. Combinatorial bionic hierarchical flexible strain sensor for sign language recognition with machine learning. *ACS Appl. Mater. Interfaces* **16**, 38780–38791 (2024).
137. Ashabi, A., Sahibuddin, S. B. & Salkhordeh Haghighi, M. The systematic review of *K*-means clustering algorithm. In *Proc. 9th Int. Conf. Netw. Commun. Comput.* 13–18 (ACM, 2020).
138. Pyun, K. R. et al. Machine-learned wearable sensors for real-time hand-motion recognition: toward practical applications. *Natl Sci. Rev.* **11**, nwad298 (2024).
139. Van der Maaten, L. & Hinton, G. Visualizing data using t-SNE. *J. Mach. Learn. Res.* **9**, 2579–2605 (2008).
140. Yang, H. et al. Topographic design in wearable MXene sensors with in-sensor machine learning for full-body avatar reconstruction. *Nat. Commun.* **13**, 5311 (2022).
141. Ouyang, Q. et al. Machine learning-coupled tactile recognition with high spatiotemporal resolution based on cross-striped nanocarbon piezoresistive sensor array. *Biosens. Bioelectron.* **246**, 115873 (2024).
142. Bhavsar, H. & Panchal, M. H. A review on support vector machine for data classification. *Int. J. Adv. Res. Computer Eng. Technol.* **1**, 185–189 (2012).
143. Taunk, K., De, S., Verma, S. & Swetapadma, A. A brief review of nearest neighbor algorithm for learning and classification. In *Int. Conf. Intelligent Comput. Control Syst. (ICCS)* 1255–1260 (IEEE, 2019).
144. Liu, D. et al. Active-matrix sensing array assisted with machine-learning approach for lumbar degenerative disease diagnosis and postoperative assessment. *Adv. Funct. Mater.* **32**, 2113008 (2022).
145. Belgiu, M. & Drăguţ, L. Random forest in remote sensing: a review of applications and future directions. *ISPRS J. Photogrammetry Remote Sens.* **114**, 24–31 (2016).
146. Tavassolian, M., Cuthbert, T. J., Napier, C., Peng, J. & Menon, C. Textile-based inductive soft strain sensors for fast frequency movement and their application in wearable devices measuring multiaxial hip joint angles during running. *Adv. Intell. Syst.* **2**, 1900165 (2020).
147. Chen, A. et al. Machine-learning enabled wireless wearable sensors to study individuality of respiratory behaviors. *Biosens. Bioelectron.* **173**, 112799 (2021).
148. Chen, J. et al. A parallel random forest algorithm for big data in a spark cloud computing environment. *IEEE Trans. Parallel Distrib. Syst.* **28**, 919–933 (2016).
149. LeCun, Y., Bengio, Y. & Hinton, G. Deep learning. *Nature* **521**, 436–444 (2015).
150. Singh, J. & Banerjee, R. A Study on single and multi-layer perceptron neural network. In *3rd Int. Conf. Comput. Methodol. Commun. (ICCMC)* 35–40 (IEEE, 2019).
151. Yu, H., Liu, Y., Zhou, G. & Peng, M. Multilayer perceptron algorithm-assisted flexible piezoresistive PDMS/chitosan/cMWCNT sponge pressure sensor for sedentary healthcare monitoring. *ACS Sens.* **8**, 4391–4401 (2023).
152. Duan, S. et al. Machine-learned, waterproof MXene fiber-based glove platform for underwater interactivities. *Nano Energy* **91**, 106650 (2022).
153. Alzubaidi, L. et al. Review of deep learning: concepts, CNN architectures, challenges, applications, future directions. *J. Big Data* **8**, 1–74 (2021).
154. Yang, A., Yang, X., Wu, W., Liu, H. & Zhuansun, Y. Research on feature extraction of tumor image based on convolutional neural network. *IEEE Access* **7**, 24204–24213 (2019).
155. Zavanelli, N., Kwon, K. & Yeo, W.-H. Printed strain sensors for motion recognition: a review of materials, fabrication methods, and machine learning algorithms. *IEEE Open J. Eng. Med. Biol.* https://doi.org/10.1109/OJEMB.2023.3330290 (2023).
156. Jogin, M., Madhulika, M., Divya, G., Meghana, R. & Apoorva, S. Feature extraction using convolution neural networks (CNN) and deep learning. In *3rd IEEE Int. Conf. Recent Trends Electron. Inform. Commun. Technol. (RTEICT)* 2319–2323 (IEEE, 2018).
157. Hüsken, M. & Stagge, P. Recurrent neural networks for time series classification. *Neurocomputing* **50**, 223–235 (2003).
158. Kim, K. K. et al. A deep-learned skin sensor decoding the epicentral human motions. *Nat. Commun.* **11**, 2149 (2020).
159. Tashakori, A. et al. Capturing complex hand movements and object interactions using machine learning-powered stretchable smart textile gloves. *Nat. Mach. Intell.* **6**, 106–118 (2024).
160. Zha, Q., Xu, Z., Cai, X., Zhang, G. & Shen, X. Wearable rehabilitation wristband for distal radius fractures. *Front. Neurosci.* **17**, 1238176 (2023).
161. Li, Y., Zhang, J., Yi, J. & Zhang, K. Convolutional-generative adversarial network: data-driven mechanical inverse method for intelligent tactile perception. *Adv. Intell. Syst.* **4**, 2100187 (2022).
162. Kim, K. K. et al. A substrate-less nanomesh receptor with meta-learning for rapid hand task recognition. *Nat. Electron.* **6**, 64–75 (2023).
163. Esposito, D. et al. A piezoresistive array armband with reduced number of sensors for hand gesture recognition. *Front. Neurorobot.* **13**, 114 (2020).
164. Wang, A. et al. Piezoresistive-based gait monitoring technique for the recognition of knee osteoarthritis patients. *IEEE Access* **10**, 123874–123884 (2022).
165. Maqsood, S., Xu, S., Springer, M. & Mohawesh, R. A benchmark study of machine learning for analysis of signal feature extraction techniques for blood pressure estimation using photoplethysmography (PPG). *IEEE Access* **9**, 138817–138833 (2021).
166. Kaisti, M. et al. Clinical assessment of a non-invasive wearable MEMS pressure sensor array for monitoring of arterial pulse waveform, heart rate and detection of atrial fibrillation. *npj Dig. Med.* **2**, 39 (2019).
167. Xia, H. et al. MXene/PPy@ PDMS sponge-based flexible pressure sensor for human posture recognition with the assistance of a convolutional neural network in deep learning. *Microsyst. Nanoeng.* **9**, 155 (2023).
168. Li, Y. et al. Low-cost data glove based on deep-learning-enhanced flexible multiwalled carbon nanotube sensors for real-time gesture recognition. *Adv. Intell. Syst.* **4**, 2200128 (2022).
169. Syu, M. H., Guan, Y. J., Lo, W. C. & Fuh, Y. K. Biomimetic and porous nanofiber-based hybrid sensor for multifunctional pressure sensing and human gesture identification via deep learning method. *Nano Energy* **76**, 105029 (2020).
170. Hang, C.-Z. et al. Highly stretchable and self-healing strain sensors for motion detection in wireless human–machine interface. *Nano Energy* **76**, 105064 (2020).
171. Jeong, Y. R. et al. A skin-attachable, stretchable integrated system based on liquid GaInSn for wireless human motion monitoring with multi-site sensing capabilities. *NPG Asia Mater.* **9**, e443 (2017).
172. Brennan, D. & Galvin, P. Evaluation of a machine learning algorithm to classify ultrasonic transducer misalignment and deployment using TinyML. *Sensors* **24**, 560 (2024).
173. Yuan, J., Zhang, Y., Wei, C. & Zhu, R. A fully self-powered wearable leg movement sensing system for human health monitoring. *Adv. Sci.* **10**, 2303114 (2023).
174. Wang, M. et al. Gesture recognition using a bioinspired learning architecture that integrates visual data with somatosensory data from stretchable sensors. *Nat. Electron.* **3**, 563–570 (2020).
175. Li, Y. et al. Learning hand kinematics for Parkinson's disease assessment using a multimodal sensor glove. *Adv. Sci.* **10**, 2206982 (2023).
176. Sundaram, S. et al. Learning the signatures of the human grasp using a scalable tactile glove. *Nature* **569**, 698–702 (2019).
177. Yang, Q. et al. Mixed-modality speech recognition and interaction using a wearable artificial throat. *Nat. Mach. Intell.* **5**, 169–180 (2023).
178. Lin, M. et al. A fully integrated wearable ultrasound system to monitor deep tissues in moving subjects. *Nat. Biotechnol.* **42**, 448–457 (2024).
179. Hu, H. et al. Stretchable ultrasonic arrays for the three-dimensional mapping of the modulus of deep tissue. *Nat. Biomed. Eng.* **7**, 1321–1334 (2023).
180. Liu, H. et al. Micromesh reinforced strain sensor with high stretchability and stability for full-range and periodic human motions monitoring. *InfoMat* **6**, e12511 (2024).
181. Gong, S. et al. Hierarchically resistive skins as specific and multimetric on-throat wearable biosensors. *Nat. Nanotechnol.* **18**, 889–897 (2023).
182. Krizhevsky, A., Sutskever, I. & Hinton, G. E. ImageNet classification with deep convolutional neural networks. *Adv. Neural Inf. Process. Syst.* https://doi.org/10.1145/3065386 (2012).

183. Wang, C. et al. Monitoring of the central blood pressure waveform via a conformal ultrasonic device. *Nat. Biomed. Eng.* **2**, 687–695 (2018).
184. Nuckols, R. W. et al. Individualization of exosuit assistance based on measured muscle dynamics during versatile walking. *Sci. Robot.* **6**, eabj1362 (2021).
185. Zhang, Q., Clark, W. H., Franz, J. R. & Sharma, N. Personalized fusion of ultrasound and electromyography-derived neuromuscular features increases prediction accuracy of ankle moment during plantarflexion. *Biomed. Signal. Process. Control.* **71**, 103100 (2022).
186. Zhang, Q., Fragnito, N., Bao, X. & Sharma, N. A deep learning method to predict ankle joint moment during walking at different speeds with ultrasound imaging: a framework for assistive devices control. *Wearable Technol.* **3**, e20 (2022).
187. Pang, Y., Yang, Z., Yang, Y. & Ren, T. L. Wearable electronics based on 2D materials for human physiological information detection. *Small* **16**, 1901124 (2020).
188. Kim, J. et al. Soft wearable flexible bioelectronics integrated with an ankle-foot exoskeleton for estimation of metabolic costs and physical effort. *npj Flex. Electron.* **7**, 3 (2023).
189. Jacobs, E., Rosen, A., Berg-Johansen, B. & Wang, L. Flexible wearable nanomaterial-based sensing device for back pain and injury prevention. *IEEE Sensors Lett.* **7**, 1–4 (2023).
190. Zhang, H. et al. A flexible wearable strain sensor for human-motion detection and a human–machine interface. *J. Mater. Chem. C* **10**, 15554–15564 (2022).
191. Mousavi, S. J., Lynch, A. C., Allaire, B. T., White, A. P. & Anderson, D. E. Walking biomechanics and spine loading in patients with symptomatic lumbar spinal stenosis. *Front. Bioeng. Biotechnol.* **9**, 751155 (2021).
192. Kent, P., Laird, R. & Haines, T. The effect of changing movement and posture using motion-sensor biofeedback, versus guidelines-based care, on the clinical outcomes of people with sub-acute or chronic low back pain — a multicentre, cluster-randomised, placebo-controlled, pilot trial. *BMC Musculoskelet. Disord.* **16**, 1–19 (2015).
193. Wang, Z. et al. A flexible, stretchable and triboelectric smart sensor based on graphene oxide and polyacrylamide hydrogel for high precision gait recognition in Parkinsonian and hemiplegic patients. *Nano Energy* **104**, 107978 (2022).
194. Kim, J. et al. Soft robotic apparel to avert freezing of gait in Parkinson's disease. *Nat. Med.* **30**, 177–185 (2024).
195. Wang, K. et al. Nanowire-based soft wearable human–machine interfaces for future virtual and augmented reality applications. *Adv. Funct. Mater.* **31**, 2008347 (2021).
196. Yin, J., Hinchet, R., Shea, H. & Majidi, C. Wearable soft technologies for haptic sensing and feedback. *Adv. Funct. Mater.* **31**, 2007428 (2021).
197. Pyun, K. R., Rogers, J. A. & Ko, S. H. Materials and devices for immersive virtual reality. *Nat. Rev. Mater.* **7**, 841–843 (2022).
198. Chen, W.-D. et al. A P300 based online brain–computer interface system for virtual hand control. *J. Zhejiang Univ. Sci. C* **11**, 587–597 (2010).
199. Proto, A. et al. Measurements of generated energy/electrical quantities from locomotion activities using piezoelectric wearable sensors for body motion energy harvesting. *Sensors* **16**, 524 (2016).
200. Han, S. et al. Multiscale nanowire–microfluidic hybrid strain sensors with high sensitivity and stretchability. *npj Flex. Electron.* **2**, 16 (2018).
201. Ma, J. et al. Highly sensitive and large-range strain sensor with a self-compensated two-order structure for human motion detection. *ACS Appl. Mater. Interfaces* **11**, 8527–8536 (2019).
202. Zhou, C.-G. et al. Highly stretchable and sensitive strain sensor with porous segregated conductive network. *ACS Appl. Mater. Interfaces* **11**, 37094–37102 (2019).
203. Liu, Y. et al. All-natural phyllosilicate–polysaccharide triboelectric sensor for machine learning-assisted human motion prediction. *npj Flex. Electron.* **7**, 21 (2023).
204. Meng, Q. et al. A facile approach to fabricate highly sensitive, flexible strain sensor based on elastomeric/graphene platelet composite film. *J. Mater. Sci.* **54**, 10856–10870 (2019).
205. Alvarez, J. T. et al. Towards soft wearable strain sensors for muscle activity monitoring. *IEEE Trans. Neural Syst. Rehabilitat. Eng.* **30**, 2198–2206 (2022).
206. Tolvanen, J., Hannu, J. & Jantunen, H. Stretchable and washable strain sensor based on cracking structure for human motion monitoring. *Sci. Rep.* **8**, 13241 (2018).
207. Xue, H., Li, F., Zhao, H., Lin, X. & Zhang, T. A paper-based iontronic capacitive pressure sensor for human muscle motion monitoring. *IEEE Electron. Device Lett.* **43**, 2165–2168 (2022).
208. Wu, Y., Ma, Y., Zheng, H. & Ramakrishna, S. Piezoelectric materials for flexible and wearable electronics: a review. *Mater. Des.* **211**, 110164 (2021).
209. Xia, S., Song, S., Jia, F. & Gao, G. A flexible, adhesive and self-healable hydrogel-based wearable strain sensor for human motion and physiological signal monitoring. *J. Mater. Chem. B* **7**, 4638–4648 (2019).
210. Kim, J.-H. et al. A conformable sensory face mask for decoding biological and environmental signals. *Nat. Electron.* **5**, 794–807 (2022).
211. Kim, D., Lee, J., Park, M. K. & Ko, S. H. Recent developments in wearable breath sensors for healthcare monitoring. *Commun. Mater.* **5**, 41 (2024).
212. Zhong, J. et al. Smart face mask based on an ultrathin pressure sensor for wireless monitoring of breath conditions. *Adv. Mater.* **34**, 2107758 (2022).
213. Zhang, K. et al. Biodegradable smart face masks for machine learning-assisted chronic respiratory disease diagnosis. *ACS Sens.* **7**, 3135–3143 (2022).
214. Hwang, B.-U. et al. Transparent stretchable self-powered patchable sensor platform with ultrasensitive recognition of human activities. *ACS Nano* **9**, 8801–8810 (2015).
215. Dagdeviren, C. et al. Conformable amplified lead zirconate titanate sensors with enhanced piezoelectric response for cutaneous pressure monitoring. *Nat. Commun.* **5**, 4496 (2014).
216. Huang, S. et al. Ultraminiaturized stretchable strain sensors based on single silicon nanowires for imperceptible electronic skins. *Nano Lett.* **20**, 2478–2485 (2020).
217. Lee, S. et al. An ultrathin conformable vibration-responsive electronic skin for quantitative vocal recognition. *Nat. Commun.* **10**, 2468 (2019).
218. Dinh Le, T.-S. et al. Ultrasensitive anti-interference voice recognition by bio-inspired skin-attachable self-cleaning acoustic sensors. *ACS Nano* **13**, 13293–13303 (2019).
219. Liu, H.-C. et al. Wearable bioadhesive ultrasound shear wave elastography. *Sci. Adv.* **10**, eadk8426 (2024).
220. Xu, S., Kim, J., Walter, J. R., Ghaffari, R. & Rogers, J. A. Translational gaps and opportunities for medical wearables in digital health. *Sci. Transl. Med.* **14**, eabn6036 (2022).
221. Gregersen, H. & Kassab, G. Biomechanics of the gastrointestinal tract. *Neurogastroenterol. Motil.* **8**, 277–297 (1996).
222. Luo, Y. et al. Technology roadmap for flexible sensors. *ACS Nano* **17**, 5211–5295 (2023).
223. Chung, H. U. et al. Skin-interfaced biosensors for advanced wireless physiological monitoring in neonatal and pediatric intensive-care units. *Nat. Med.* **26**, 418–429 (2020).
224. Zhao, W. et al. High-strength, fast self-healing, aging-insensitive elastomers with shape memory effect. *ACS Appl. Mater. Interfaces* **12**, 35445–35452 (2020).
225. Kong, Z. et al. Ultrafast underwater self-healing piezo-ionic elastomer via dynamic hydrophobic–hydrolytic domains. *Nat. Commun.* **15**, 2129 (2024).
226. Son, D. et al. An integrated self-healable electronic skin system fabricated via dynamic reconstruction of a nanostructured conducting network. *Nat. Nanotechnol.* **13**, 1057–1065 (2018).
227. Zhang, B. et al. A three-dimensional liquid diode for soft, integrated permeable electronics. *Nature* **628**, 84–92 (2024).
228. Wicaksono, I. et al. A tailored, electronic textile conformable suit for large-scale spatiotemporal physiological sensing in vivo. *npj Flex. Electron.* **4**, 1–13 (2020).
229. Yuk, H. et al. Dry double-sided tape for adhesion of wet tissues and devices. *Nature* **575**, 169–174 (2019).
230. Kim, J.-H., Kim, S.-R., Kil, H.-J., Kim, Y.-C. & Park, J.-W. Highly conformable, transparent electrodes for epidermal electronics. *Nano Lett.* **18**, 4531–4540 (2018).
231. Rothberg, J. M. et al. Ultrasound-on-chip platform for medical imaging, analysis, and collective intelligence. *Proc. Natl Acad. Sci. USA* **118**, e2019339118 (2021).
232. Bharath, R. et al. FPGA-based portable ultrasound scanning system with automatic kidney detection. *J. Imaging* **1**, 193–219 (2015).
233. Wu, Y.-D., Ruan, S.-J. & Lee, Y.-H. An ultra-low power surface EMG sensor for wearable biometric and medical applications. *Biosensors* **11**, 411 (2021).
234. Lv, D., Jiang, Q., Shang, Y. & Liu, D. Highly efficient fiber-shaped organic solar cells toward wearable flexible electronics. *npj Flex. Electron.* **6**, 38 (2022).
235. Hwang, G. T. et al. Self-powered wireless sensor node enabled by an aerosol-deposited PZT flexible energy harvester. *Adv. Energy Mater.* **6**, 1600237 (2016).
236. Li, J., Yin, J., Wee, M. G. V., Chinnappan, A. & Ramakrishna, S. A self-powered piezoelectric nanofibrous membrane as wearable tactile sensor for human body motion monitoring and recognition. *Adv. Fiber Mater.* **5**, 1417–1430 (2023).
237. Jung, Y. H. et al. A wireless haptic interface for programmable patterns of touch across large areas of the skin. *Nat. Electron.* **5**, 374–385 (2022).
238. Tekin, N., Aris, A., Acar, A., Uluagac, S. & Gungor, V. C. A review of on-device machine learning for IoT: an energy perspective. *Ad Hoc Netw.* **153**, 103348 (2023).
239. Vohra, S. K., Thomas, S. A., Sakare, M. & Das, D. M. Circuit implementation of on-chip trainable spiking neural network using CMOS based memristive STDP synapses and LIF neurons. *Integration* **95**, 102122 (2024).
240. Milo, V., Malavena, G., Monzio Compagnoni, C. & Ielmini, D. Memristive and CMOS devices for neuromorphic computing. *Materials* **13**, 166 (2020).
241. Sebastian, A., Le Gallo, M., Khaddam-Aljameh, R. & Eleftheriou, E. Memory devices and applications for in-memory computing. *Nat. Nanotechnol.* **15**, 529–544 (2020).
242. Han, S., Mao, H. & Dally, W. J. Deep compression: compressing deep neural networks with pruning, trained quantization and Huffman coding. In *4th Int. Conf. Learning Represent.* (2016).
243. Iandola, F. N. et al. SqueezeNet: AlexNet-level accuracy with 50× fewer parameters and <0.5 MB model size. Preprint at https://arxiv.org/abs/1602.07360 (2016).
244. Inertial Labs. Advantages and disadvantages of inertial measurement units. *Inertial Labs* https://inertiallabs.com/advantages-and-disadvantages-of-inertial-measurement-units/#:~:text=The%20accuracy%20of%20IMU%20measurements,also%20be%20affected%20by%20noise (2024).
245. Roach, K. E. & Miles, T. P. Normal hip and knee active range of motion: the relationship to age. *Phys. Ther.* **71**, 656–665 (1991).
246. Pham, T., Pathirana, P. N., Trinh, H. & Fay, P. A non-contact measurement system for the range of motion of the hand. *Sensors* **15**, 18315–18333 (2015).
247. Zhang, X. & Huang, H. A real-time, practical sensor fault-tolerant module for robust EMG pattern recognition. *J. Neuroeng. Rehabil.* **12**, 1–16 (2015).
248. Meng, K. et al. Wearable pressure sensors for pulse wave monitoring. *Adv. Mater.* **34**, 2109357 (2022).
249. Fine, J. et al. Sources of inaccuracy in photoplethysmography for continuous cardiovascular monitoring. *Biosensors* **11**, 126 (2021).
250. Gao, X. et al. A photoacoustic patch for three-dimensional imaging of hemoglobin and core temperature. *Nat. Commun.* **13**, 7757 (2022).
251. Boutry, C. M. et al. Biodegradable and flexible arterial-pulse sensor for the wireless monitoring of blood flow. *Nat. Biomed. Eng.* **3**, 47–57 (2019).
252. Mathew, J., Zheng, D., Xu, J. & Liu, H. Systematic review on fabrication, properties, and applications of advanced materials in wearable photoplethysmography sensors. *Adv. Electron. Mater.* **10**, 230065 (2024).

253. Yang, S. & Lu, N. Gauge factor and stretchability of silicon-on-polymer strain gauges. *Sensors* **13**, 8577–8594 (2013).
254. Lin, H., Zhang, C., Liao, N. & Zhang, M. Microcracked strain sensor based on carbon nanotubes/copper composite film with high performance and waterproof property for underwater motion detection. *Compos. B Eng.* **254**, 110574 (2023).
255. Lin, Z. et al. Insights into materials, physics, and applications in flexible and wearable acoustic sensing technology. *Adv. Mater.* **36**, 2306880 (2024).
256. Yang, T. et al. Mechanical sensors based on two-dimensional materials: sensing mechanisms, structural designs and wearable applications. *iScience* **25**, 103728 (2022).
257. Ismail, S. N. A., Nayan, N. A., Mohammad Haniff, M. A. S., Jaafar, R. & May, Z. Wearable two-dimensional nanomaterial-based flexible sensors for blood pressure monitoring: a review. *Nanomaterials* **13**, 852 (2023).
258. He, Y., Cheng, Y., Yang, C. & Guo, C. F. Creep-free polyelectrolyte elastomer for drift-free iontronic sensing. *Nat. Mater.* **23**, 1107–1114 (2024).
259. Qin, Q., Cao, X. & Wang, N. Ball-mill-inspired durable triboelectric nanogenerator for wind energy collecting and speed monitoring. *Nanomaterials* **13**, 939 (2023).
260. Kim, W., Yasmeen, S., Nguyen, C. T., Lee, H.-B.-R. & Choi, D. Toward enhanced humidity stability of triboelectric mechanical sensors via atomic layer deposition. *Nanomaterials* **11**, 1795 (2021).
261. Wang, Y., Yu, Y., Wei, X. & Narita, F. Self-powered wearable piezoelectric monitoring of human motion and physiological signals for the postpandemic era: a review. *Adv. Mater. Technol.* **7**, 2200318 (2022).
262. Dcosta, J. V., Ochoa, D. & Sanaur, S. Recent progress in flexible and wearable all organic photoplethysmography sensors for SpO_2 monitoring. *Adv. Sci.* **10**, 2302752 (2023).
263. Lee, G. H. et al. Stretchable PPG sensor with light polarization for physical activity-permissible monitoring. *Sci. Adv.* **8**, eabm3622 (2022).
264. Lee, S. H. et al. Fully portable continuous real-time auscultation with a soft wearable stethoscope designed for automated disease diagnosis. *Sci. Adv.* **8**, eabo5867 (2022).
265. Gupta, P. et al. Precision wearable accelerometer contact microphones for longitudinal monitoring of mechano-acoustic cardiopulmonary signals. *npj Digit. Med.* **3**, 19 (2020).
266. Chen, L. Y. et al. Continuous wireless pressure monitoring and mapping with ultra-small passive sensors for health monitoring and critical care. *Nat. Commun.* **5**, 5028 (2014).
267. Lee, H. J. et al. Hetero-dimensional 2D $Ti_3C_2T_x$ MXene and 1D graphene nanoribbon hybrids for machine learning-assisted pressure sensors. *ACS Nano* **15**, 10347–10356 (2021).
268. Li, X. et al. Electret-based flexible pressure sensor for respiratory diseases auxiliary diagnosis system using machine learning technique. *Nano Energy* **114**, 108652 (2023).
269. Liu, S., Rao, Y., Jang, H., Tan, P. & Lu, N. Strategies for body-conformable electronics. *Matter* **5**, 1104–1136 (2022).
270. Sunwoo, S.-H., Ha, K.-H., Lee, S., Lu, N. & Kim, D.-H. Wearable and implantable soft bioelectronics: device designs and material strategies. *Annu. Rev. Chem. Biomol. Eng.* **12**, 359–391 (2021).
271. Yoon, H. et al. Adaptive epidermal bioelectronics by highly breathable and stretchable metal nanowire bioelectrodes on electrospun nanofiber membrane. *Adv. Funct. Mater.* **34**, 2313504 (2024).
272. Wyser, Y., Pelletier, C. & Lange, J. Predicting and determining the bending stiffness of thin films and laminates. *Packag. Technol. Sci.* **14**, 97–108 (2001).
273. Hou, J. F. et al. An implantable piezoelectric ultrasound stimulator (ImPULS) for deep brain activation. *Nat. Commun.* **15**, 4601 (2024).
274. Jeong, S. H., Shou, Z., Hjort, K., Hilborn, J. & Wu, Z. PDMS-based elastomer tuned soft, stretchable, and sticky for epidermal electronics. *Adv. Mater.* **28**, 5830–5836 (2016).
275. Darby, D. R., Cai, Z., Mason, C. R. & Pham, J. T. Modulus and adhesion of Sylgard 184, Solaris, and Ecoflex 00-30 silicone elastomers with varied mixing ratios. *J. Appl. Polym. Sci.* **139**, e52412 (2022).
276. Luo, F. et al. Oppositely charged polyelectrolytes form tough, self-healing, and rebuildable hydrogels. *Adv. Mater.* **27**, 2722–2727 (2015).
277. Liang, Y., Xue, J., Du, B. & Nie, J. Ultrastiff, tough, and healable ionic–hydrogen bond cross-linked hydrogels and their uses as building blocks to construct complex hydrogel structures. *ACS Appl. Mater. Interfaces* **11**, 5441–5454 (2019).
278. Zhou, T. et al. 3D printable high-performance conducting polymer hydrogel for all-hydrogel bioelectronic interfaces. *Nat. Mater.* **22**, 895–902 (2023).
279. Yu, J. et al. Design of highly conductive, intrinsically stretchable, and 3D printable PEDOT: PSS hydrogels via PSS-chain engineering for bioelectronics. *Chem. Mater.* **35**, 5936–5944 (2023).
280. Sirohi, J. & Chopra, I. Fundamental understanding of piezoelectric strain sensors. *J. Intell. Mater. Syst. Struct.* **11**, 246–257 (2000).
281. Ayed, A. B., Bouhamed, A., Abdelmoula, N., Khemakhem, H. & Kanoun, O. Enhanced dielectric and mechanical properties of PVDF-HFP/Zn-BCZT composite. In 19*th Int. Multi-Conf. Syst. Signals Devices (SSD)* 1710–1714 (IEEE, 2022).
282. Jeong, J.-W. et al. Materials and optimized designs for human–machine interfaces via epidermal electronics. *Adv. Mater.* **25**, 6839–6846 (2013).
283. Carovac, A., Smajlovic, F. & Junuzovic, D. Application of ultrasound in medicine. *Acta Inform. Med.* **19**, 168 (2011).
284. Martin, K. in *Diagnostic Ultrasound* 3rd edn 1–5 (CRC, 2019).
285. Bunce, S. M., Hough, A. D. & Moore, A. P. Measurement of abdominal muscle thickness using M-mode ultrasound imaging during functional activities. *Man. Ther.* **9**, 41–44 (2004).
286. Hoskins, P. R. in *Diagnostic Ultrasound* 3rd edn 143–158 (CRC, 2019).
287. Routh, H. F. Doppler ultrasound. *IEEE Eng. Med. Biol. Mag.* **15**, 31–40 (1996).

Acknowledgements

This work was supported by the MIT Media Lab Consortium funding. This work was also supported by the National Research Foundation of Korea (Grant No. 2021R1A2B5B03001691). H.Y. acknowledges the support by the Korean Government Scholarship Program for Study Overseas fellowship from National Institute for International Education, Korea.

Author contributions

H.Y. and J.-H.K. contributed equally to all aspects of the article. H.Y., J.-H.K. and C.D. researched data and wrote the manuscript. All authors contributed substantially to discussion of the content. All authors reviewed and/or edited the manuscript before submission.

Competing interests

The authors declare no competing interests.

Additional information

Supplementary information The online version contains supplementary material available at https://doi.org/10.1038/s41578-024-00729-3.

Peer review information *Nature Reviews Materials* thanks Kilwon Cho, Naoji Matsuhisa, Sheng Xu and the other, anonymous, reviewer(s) for their contribution to the peer review of this work.